RAP1-mediated MEK/ERK pathway defects in Kabuki syndrome

Nina Bögershausen,[1,2,3] I-Chun Tsai,[4] Esther Pohl,[1,2,3] Pelin Özlem Simsek Kiper,[5] Filippo Beleggia,[1,2,3] E. Ferda Percin,[6] Katharina Keupp,[1,2,3] Angela Matchan,[7] Esther Milz,[1,2,3] Yasemin Alanay,[5,8] Hülya Kayserili,[9] Yicheng Liu,[1,2,3] Siddharth Banka,[10] Andrea Kranz,[11] Martin Zenker,[12] Dagmar Wieczorek,[13] Nursel Elcioglu,[14] Paolo Prontera,[15] Stanislas Lyonnet,[16] Thomas Meitinger,[17] A. Francis Stewart,[11] Dian Donnai,[10] Tim M. Strom,[17,18] Koray Boduroglu,[5] Gökhan Yigit,[1,2,3] Yun Li,[1,2,3] Nicholas Katsanis,[4] and Bernd Wollnik[1,2,3]

[1]Institute of Human Genetics, [2]Center for Molecular Medicine Cologne (CMMC), and [3]Cologne Excellence Cluster on Cellular Stress Responses in Aging-Associated Diseases (CECAD), University of Cologne, Cologne, Germany. [4]Center for Human Disease Modeling and Department of Cell Biology, Duke University, Durham, North Carolina, USA. [5]Pediatric Genetics Unit, Department of Pediatrics, Hacettepe University Medical Faculty, Ankara, Turkey. [6]Department of Medical Genetics, Gazi University Faculty of Medicine, Ankara, Turkey. [7]Oxford Gene Technology (OGT), Begbroke Science Park, Begbroke, Oxfordshire, United Kingdom. [8]Pediatric Genetics, Department of Pediatrics, Acibadem University, School of Medicine, Istanbul, Turkey. [9]Medical Genetics Department, Koç University, School of Medicine, Istanbul, Turkey. [10]Department of Genetic Medicine, St. Mary's Hospital, Manchester Academic Health Sciences Centre (MAHSC), University of Manchester, Manchester, United Kingdom. [11]Genomics, Bio-Innovationszentrum, Dresden University of Technology, Dresden, Germany. [12]Institute of Human Genetics, University Hospital Magdeburg, Magdeburg, Germany. [13]Institut für Humangenetik, Universitätsklinikum Essen, Essen, Germany. [14]Department of Pediatric Genetics, Marmara University Medical Faculty, Istanbul, Turkey. [15]Medical Genetics Unit, Hospital and University of Perugia, Perugia, Italy. [16]Université Paris Descartes-Sorbonne Paris Cité, Institut Imagine, INSERM U781, Hôpital Necker-Enfants Malades, Paris, France. [17]Institute of Human Genetics, Helmholtz Zentrum München, Neuherberg, Germany. [18]Institute of Human Genetics, Technische Universität München, Munich, Germany.

The genetic disorder Kabuki syndrome (KS) is characterized by developmental delay and congenital anomalies. Dominant mutations in the chromatin regulators lysine (K)–specific methyltransferase 2D (*KMT2D*) (also known as *MLL2*) and lysine (K)–specific demethylase 6A (*KDM6A*) underlie the majority of cases. Although the functions of these chromatin-modifying proteins have been studied extensively, the physiological systems regulated by them are largely unknown. Using whole-exome sequencing, we identified a mutation in *RAP1A* that was converted to homozygosity as the result of uniparental isodisomy (UPD) in a patient with KS and a de novo, dominant mutation in *RAP1B* in a second individual with a KS-like phenotype. We elucidated a genetic and functional interaction between the respective KS-associated genes and their products in zebrafish models and patient cell lines. Specifically, we determined that dysfunction of known KS genes and the genes identified in this study results in aberrant MEK/ERK signaling as well as disruption of F-actin polymerization and cell intercalation. Moreover, these phenotypes could be rescued in zebrafish models by rebalancing MEK/ERK signaling via administration of small molecule inhibitors of MEK. Taken together, our studies suggest that the KS pathophysiology overlaps with the RASopathies and provide a potential direction for treatment design.

Introduction

De novo dominant germline mutations in lysine (K)–specific methyltransferase 2D (*KMT2D*; formerly *MLL2, ALR*; ref. 1) or lysine (K)–specific demethylase 6A (*KDM6A*) cause Kabuki syndrome (KS; MIM 147920 and 300867; refs. 2–4), a developmental disorder characterized by a recognizable facial gestalt, intellectual disability, and short stature as well as cardiac, renal, and skeletal malformations (5). *KMT2D* mutations are the major cause of KS, present in up to 75% of patients (6), while *KDM6A* mutations account for roughly 5% of cases (7). Consequently, for the residual 20% of patients, the genetic cause of the disorder remains unresolved.

KMT2D encodes a methyltransferase of the trithorax group, responsible for histone 3 lysine 4 (H3K4) di- and trimethylation (8), which is a hallmark of active transcription states that counteract the influence of the repressive polycomb group proteins (9). *KMT2D* interacts closely with several proteins, building a multiprotein complex that also includes the proteins RBBP5 and KDM6A (10, 11). KDM6A is a histone 3 lysine 27 (H3K27) demethylase, responsible for polycomb mark removal (12), a crucial step in the complex function of the KMT2D-containing complex, also known as ASCOM. The majority of mutations found in *KMT2D* and *KDM6A* in patients with KS are heterozygous truncating mutations that completely abolish enzyme activity (4). It has been shown that truncating mutations in *KMT2D* lead to nonsense-mediated mRNA decay (NMD) and significantly reduced KMT2D protein levels (13). In the case of *KDM6A*, whole-gene deletions have been described. Hence, mutations in the known KS genes most likely result in haploinsufficiency. Although altered

Authorship note: Nina Bögershausen and I-Chun Tsai contributed equally to this work.
Note regarding evaluation of this manuscript: Manuscripts authored by scientists associated with Duke University, The University of North Carolina at Chapel Hill, Duke-NUS, and the Sanford-Burnham Medical Research Institute are handled not by members of the editorial board but rather by the science editors, who consult with selected external editors and reviewers.
Conflict of interest: The authors have declared that no conflict of interest exists.
Submitted: November 20, 2014; **Accepted:** July 9, 2015.
Reference information: *J Clin Invest*. 2015;125(9):3585–3599. doi:10.1172/JCI80102.

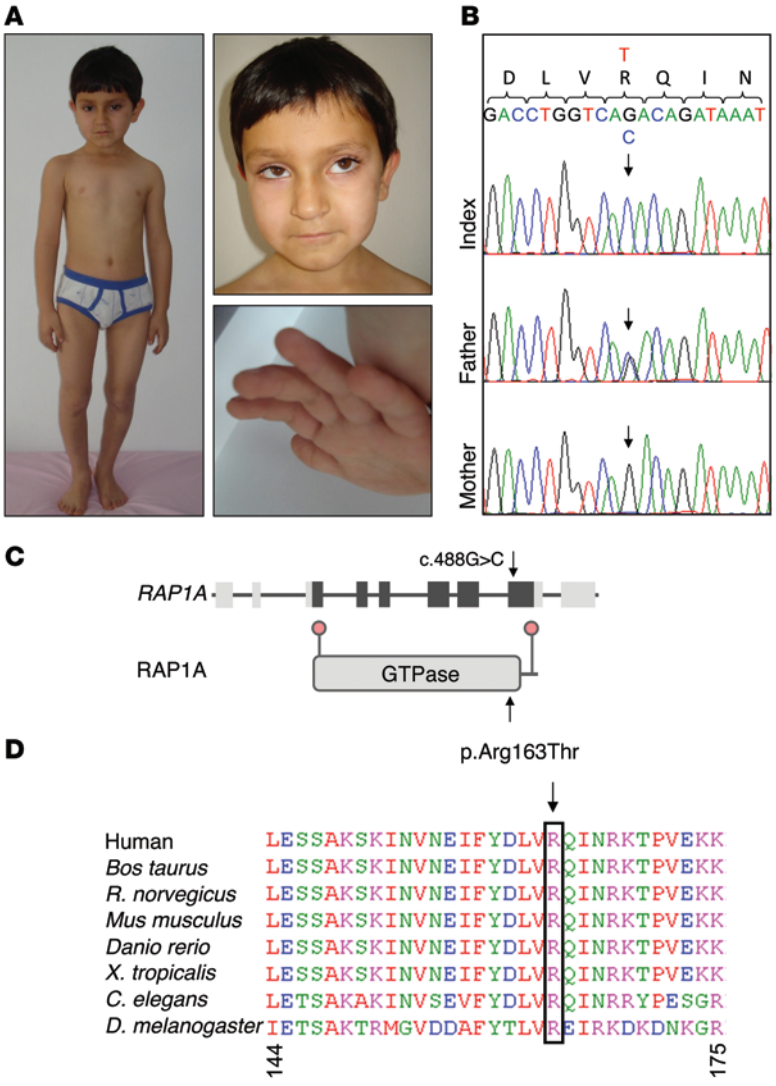

Figure 1. The de novo mutation c.488G>C (p.Arg163Thr) in *RAP1A* identified in a patient with KS. (**A**) Clinical presentation. Left: note the proportionate short stature, short neck, and shoulder asymmetry as a result of Sprengel's deformity. Upper right: facial features indicative of KS: wide palpebral fissures, long eyelashes, arched, flared eyebrows, large ears, flat midface, and full cheeks. Lower right: hand of the patient with persistent fingertip pads. (**B**) Sanger sequencing confirmation of the *RAP1A* c.488G>C mutation showing homozygosity in the patient due to UPD. (**C**) Schematic representation of the *RAP1A* gene and the RAP1A protein; black arrows indicate the localization of the identified homozygous missense mutation. (**D**) The affected amino acid residue is highly conserved among a wide range of species.

expression of target genes has been shown (13), the downstream pathomechanism of KS has not yet been elucidated.

RAP1A, and the highly related protein RAP1B (95% amino acid identity), belong to the Ras family of small GTPases, regulating various cellular processes such as cell adhesion and migration (14–16); studies in *Xenopus* and zebrafish have shown that *rap1a* and *rap1b* morphants exhibit similar gastrulation defects, highlighting the important role of both proteins in early development (17). RAP1 is known to exert opposing effects on the MAPK pathway (18), depending on tissue- and cell-specific context: an activating effect through BRAF (19, 20) and a repressive effect through RAF1 (21).

In this study, we link RAP1A and RAP1B to KS and identify the KMT2D-containing ASCOM complex as a major regulator of the MEK/ERK pathway, thus providing insight into the molecular mechanisms underlying KS.

Results

We performed trio whole-exome sequencing in a KS patient negative for mutations in the known KS genes (Figure 1A and Table 1). Filtering for Mendelian violations did not identify any pathogenic de novo variants, and screening for possible recessive alleles did not produce a likely candidate. However, we observed paternal uniparental isodisomy (UPD) for chromosome 1, which was confirmed by microsatellite marker analysis of chromosome 1 (Figure 2A). Filtering the UPD region for coding alleles with a minor allele frequency (MAF) of less than 1% led to the identification of 12 novel homoallelic variants (Supplemental Figure 1; supplemental material available online with this article; doi:10.1172/JCI80102DS1). The missense variant c.488G>C in *RAP1A* was located within the region of a 12-Mb duplication of chromosome 1p13.1-p22.1 previously identified in a KS patient (22) and was predicted to alter protein function (PolyPhen-2: http://genetics.bwh.harvard.edu/pph2/; PROVEAN: http://provean.jcvi.org/index.php) (Supplemental Figure 1). Sanger sequencing confirmed the heterozygous carrier status in the father, while the index patient was homozygous, lacking a maternal WT allele (Figure 1B). The c.488G>C variant is predicted to change the conserved arginine at position 163, located close to the phosphorylation site at serine 180 (Human Protein Reference Database: http://www.hprd.org/), to threonine (Figure 1, C and D, and Supplemental Figure 2A). We did not find this change in 270 ethnically matched control individuals, nor was it present in any available control data sets such as 1000 Genomes (1KG; http://www.1000genomes.org/), the approximately 13,000 chromosomes in the Exome Variant Server (EVS; http://evs.gs.washington.edu/EVS/), or the approximately 120,000 alleles in the Exome Aggregation Consortium browser (ExAC; http://exac.broadinstitute.org/). Notably, there was no loss-of-function mutation found in *RAP1A* in any individual in ExAC, suggesting that this gene is under strong negative selection. Neither Sanger sequencing of all *RAP1A*-coding exons nor quantitative PCR detected another pathogenic mutation or structural variant in 78 additional *KMT2D* mutation–negative KS patients, suggesting that *RAP1A* is a rare contributor to KS.

To evaluate the candidacy of RAP1A in our patient, we tested whether the mutation might affect RAP1A activity. We first purified GTP-bound RAP1A (mutant or WT) with RalGDS-RBD beads (23); although the overall protein amounts of the mutant protein were not altered appreciably, we observed a reduction of active, GTP-bound RAP1A after stimulation of cells with EGF (Figure 2B), suggesting a loss-of-function mechanism. Since

Table 1. Clinical findings in patients with *RAP1A/RAP1B* mutations

Symptom	Frequency in KS[A]	*RAP1A* patient	*RAP1B* patient
Growth anomalies	68%	+	+
Short stature	58%	+	+
Microcephaly	58%	+	+
Developmental anomalies	95%	+	+
Developmental delay	95%	+	+
Feeding difficulties	68%	–	–
Muscular hypotonia	82%	–	–
Facial dysmorphism	95%	+	+
Typical facial gestalt	89%	+	–
Long palpebral fissures	95%	+	+
Eversion lateral lower eyelid	79%	+	–
Arched eyebrows	89%	+	+
Long, dense eyelashes	89%	+	+
Dysplastic ears	95%	+	+
Cleft palate	16%	–	–
Strabismus	32%	+	+
Renal anomalies	41%	–	–
Renal malformation	24%	–	–
Hydronephrosis	24%	–	–
Congenital heart defects	47%	–	+
ASD/VSD	30%	–	–
PDA/PFO	24%	–	–
Other	18%	–	+
Others			
Fetal finger pads	90%	+	–
Frequent otitis	47%	–	–
Early puberty	7%	–	–
Cryptorchidism	21%	–	–
Seizures/abnormal EEG	5%	+	+
Skeletal findings	80%[B]	Joint hyperlaxity Sprengel's deformity	Right tibial shortening Brachyphalangy

ASD, atrial septal defect; VSD, ventricular septal defect; PDA, patent ductus arteriosus; PFO, patent foramen ovale. [A]Ref. 49. [B]Ref. 50.

we saw residual basal activity, it is possible that p.Arg163Thr is a hypomorphic allele. We next tested the effect of the RAP1A variant in a zebrafish model. Given the redundancy between *rap1a* and *rap1b* during gastrulation, we injected morpholinos (MOs) silencing both *rap1a* and *rap1b* and we scored 50 to 100 embryos/injection for convergent-extension (CE) defects (blind to injection cocktail) according to previously established criteria (class I embryos have grossly normal morphology, but are shorter than control-injected embryos at the same somatic age; class II embryos are shorter and thinner than class I embryos and have poorly developed head, eye, and tail structure, with poor somatic definition and symmetry; ref. 24). We observed CE defects that could be rescued by coinjection of $rap1^{MO}$ with 0.5 pg of WT human *RAP1A* mRNA ($RAP1A^{WT}$; $P < 0.0001$). In agreement with our in vitro data, coinjection of $rap1^{MO}$ with a human *RAP1A* mRNA encoding p.Arg163Thr ($RAP1A^{R163T}$) was significantly worse than WT ($P < 0.0001$), but indistinguishable from $rap1^{MO}$, providing a second line of evidence that p.Arg163Thr is a loss-of-function allele (Figure 2C and Supplemental Figure 2C). To assess this effect by objective quantitative measurements, we performed in situ labeling of embryos with a riboprobe cocktail against *myoD*, *pax2*, and *krox20*, and we measured the ratio of the distal ends of the fifth somite (width [W]) versus the length of the notochord (length [L]). Consistent with a CE defect, depletion of *rap1* increased the W/L ratio, which can be rescued by human $RAP1A^{WT}$, but not by $RAP1A^{R163T}$ mRNA (Figure 2D). Additionally, to ascertain the specificity of the CE defects, we tested whether deletion of *rap1a*, *rap1b*, or both in the same genome would reproduce the $rap1^{MO}$ phenotypes. We therefore induced deletions in each gene by *CAS9*/gRNA (25). In the F0 generation, we observed CE defects in 45% and 20% of embryos for *rap1a* and *rap1b*, respectively; combinatorial injection of guide RNAs for both genes induced CE defects in approximately 70% of embryos (Figure 3A). Genotyping of 24 double-mutant embryos showed changes for 22 and 21 embryos for *rap1a* and *rap1b*, respectively (Figure 3, B and C). These data, together with the rescue of the CE defects with WT mRNA, showed that the phenotype is specific to the targeted genes.

Since our data suggest that mutations in *RAP1A* are likely causative of KS, we speculated that the closely related gene *RAP1B* might also be involved in the etiopathology of KS. Initial analysis of our KS cohort ($n = 78$) did not identify likely pathogenic point mutations or structural variants. However, we identified a de novo mutation in *RAP1B* (c.451A>G; p.Lys151Glu) by trio whole-exome sequencing (Supplemental Table 1) in a patient initially diagnosed with Hadziselimovic syndrome (MIM 612946), a disorder that overlaps clinically with KS. Careful clinical reevaluation revealed that the patient's phenotype fits the KS spectrum (Table 1, Figure 4A, and Supplemental Table 2). The c.451A>G allele (Figure 4B) was absent from all databases (1KG, EVS, and ExAC) and was predicted computationally to be deleterious. The conserved lysine 151 (Figure 4C) is located close to the GTP-binding site of RAP1B (Supplemental Figure 2B). We tested the activity of this *RAP1B* allele using the in vivo CE complementation assay: *RAP1B* mRNA encoding Glu at position 151 failed to rescue *rap1* morphants (Figure 4, D and E) in a manner similar to the *RAP1A* mutant allele, while expression of the mutant allele in control embryos was indistinguishable from the expression of WT *RAP1B* mRNA (data not shown), likely excluding a dominant negative effect. Together, these data suggested a model of haploinsufficiency for RAP1B.

To further investigate the relevance of RAP1 signaling to KS, we set out to test whether suppression of the known KS genes *KMT2D* and *KDM6A* would phenocopy RAP1 morphants/CRISPR mutants. To this end, we generated MOs against the sole orthologs of *KMT2D* and *KDM6A*. Using the same morphometrics as for *rap1* morphants, we found that *kmt2d* and *kdm6a* morphants exhibited shorter anterior-posterior axis, wider notochord (Figure 5A), and significantly increased somitic/notochord W/L ratio ($P < 0.01$) compared with controls (Figure 5B). Although the large size of *KMT2D* rendered rescue experimentally intractable, we saw efficient suppression of *kmt2d* by reverse transcriptase–PCR (RT-PCR) (Figure 5C), and we reproduced the phenotype with a second, nonoverlapping $kmt2d^{MO}$ (Figure 5A). Coinjection of $kdm6a^{MO}$ with human $KDM6A^{WT}$ mRNA rescued CE defects, providing evidence for specificity (Figure 5A).

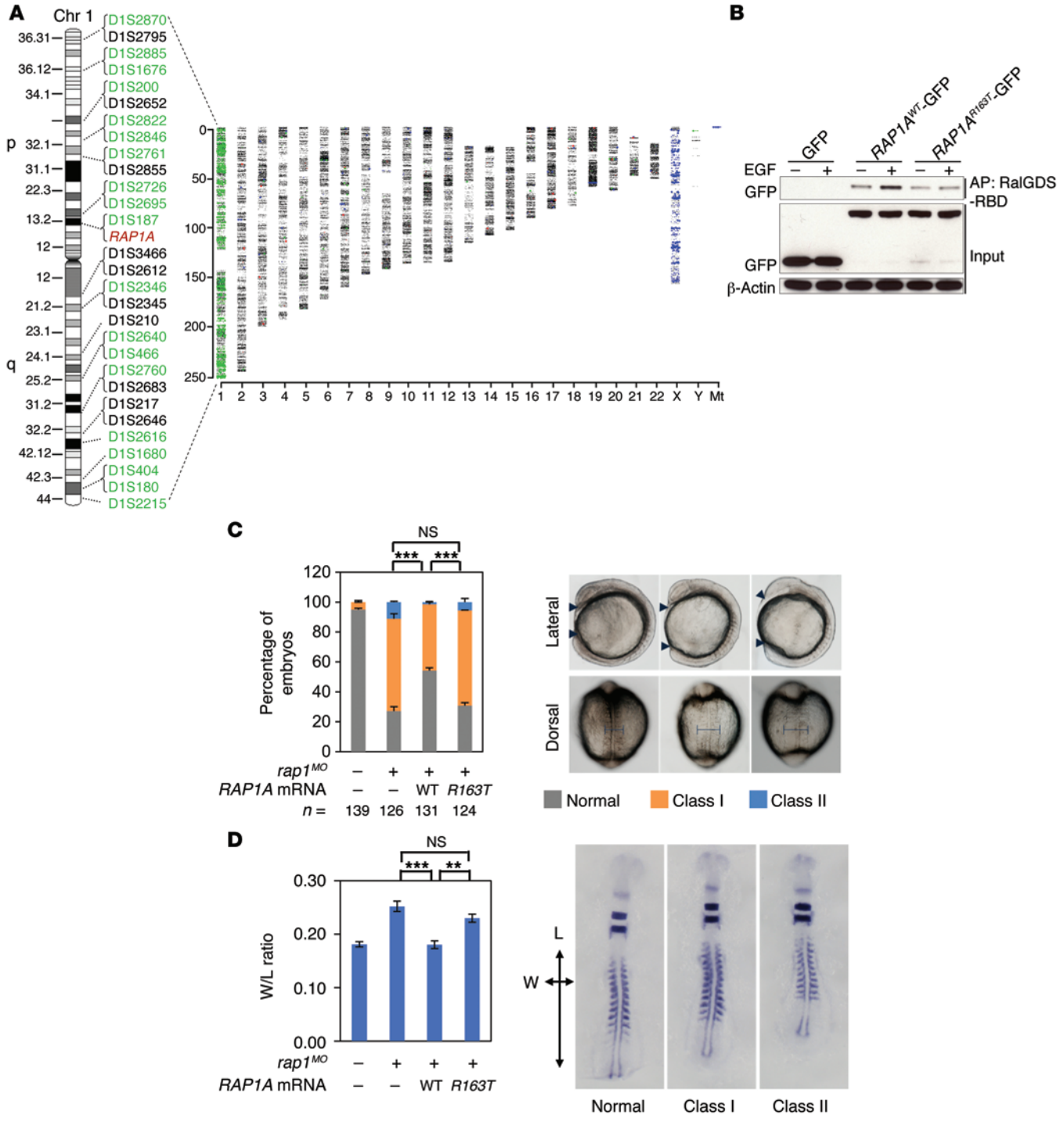

Figure 2. Uniparental disomy detection by whole-exome sequencing. (**A**) Right: variants identified by exome sequencing are plotted against chromosomes; colored dots indicate Mendelian inconsistencies (green: paternal UPD; blue: maternal UPD; male sample); left: pUPD of chromosome 1 was confirmed by microsatellite marker analysis (green: pUPD, black: homozygous). (**B**) Active RAP1 pull-down assay shows a markedly reduced activation of *RAP1A*^{R163T}-GFP after EGF stimulation compared with *RAP1A*^{WT}-GFP ($n = 4$). (**C**) MO KD of *rap1* causes CE defects in zebrafish that are partially rescued by WT, but not *RAP1A*^{R163T} mRNA. ***$P < 0.001$, χ^2 test. Error bars show SEM. Arrowheads show the body gap angle. Bars show the width of somites. (**D**) MO KD of *rap1* causes a shift in the width-length ratio of somites in zebrafish embryos that is rescued by WT but not *RAP1A*^{R163T} mRNA. Class I and class II embryos were merged for the statistical analysis. **$P < 0.01$, 2-tailed Student's *t* test ($n = 10$). Error bars show SEM.

Patients with KS may present with skeletal changes, such as brachydactyly, and defective jaw development, i.e., retrognathia, malocclusion, and/or cleft palate (5). Aberrant jaw development has been seen previously in CE mutants (26, 27). We asked whether this phenotype was common to the known and the new KS genes, and we sought to explore its mechanistic basis. We therefore examined *rap1*, *kmt2d*, and *kdm6a* morphants at 5 days post fertilization (dpf) and stained their cartilaginous structures

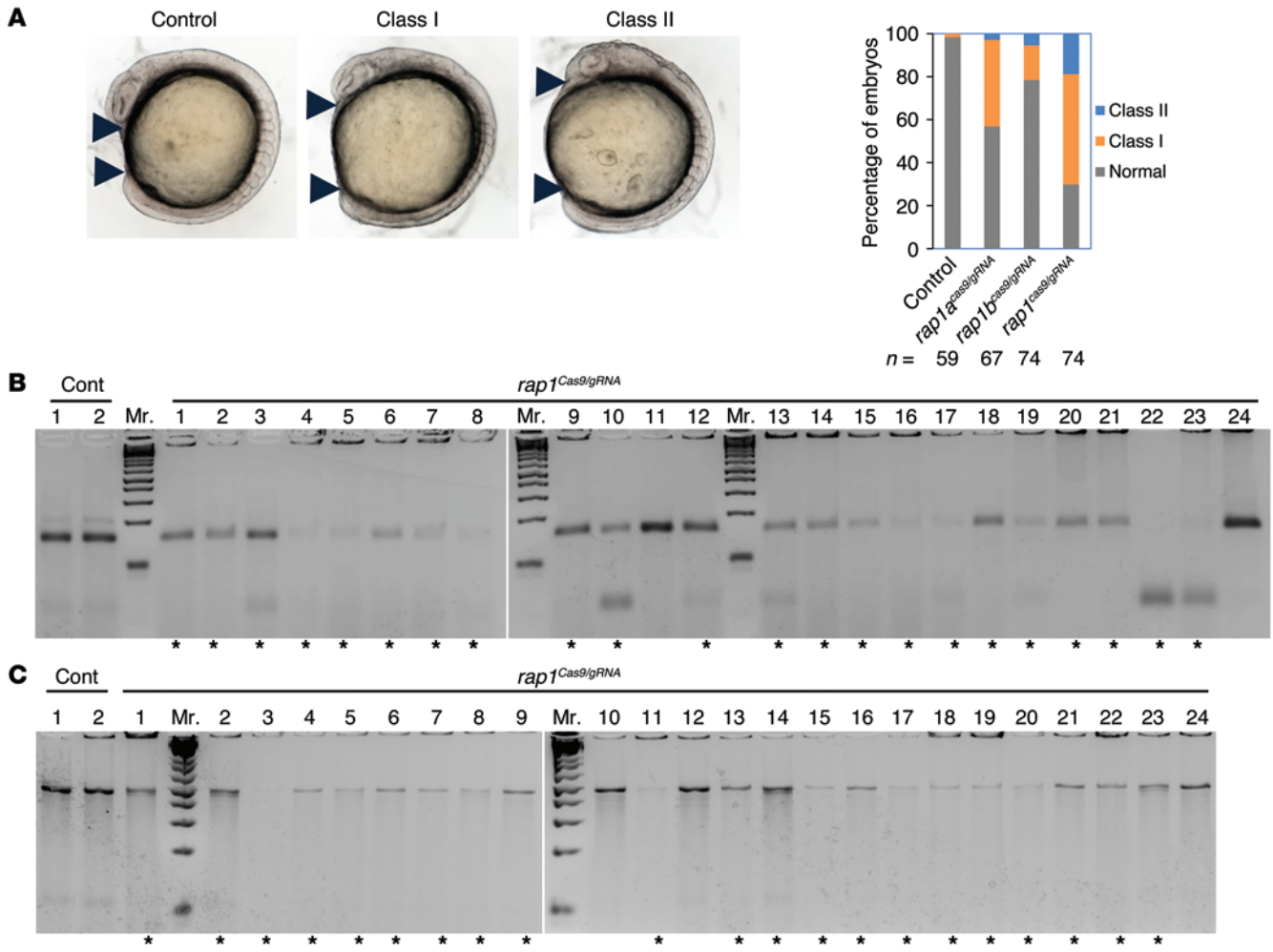

Figure 3. *Rap1*$^{Cas9/gRNA}$ embryos exhibit phenotypes similar to *rap1* morphant. (**A**) 45% and 20% CE defects were observed in embryos injected with gRNA targeting *rap1a* or *rap1b*. Combinatorial injection of guide RNAs for both genes (*rap1*$^{Cas9/gRNA}$) induced CE defects in approximately 70% of embryos. Statistical analysis used the χ^2 test. (**B**) Genotyping for genome editing of *rap1a*. Targeted clones (denoted with asterisks) are determined by appearance of size-changed band, extra band, smear, or inefficient PCR. Cont, control; Mr., marker (Invitrogen 1 kb Plus). (**C**) Genotyping for genome editing of *rap1b*. Targeted clones (denoted with asterisks) are determined by the same criteria as for *rap1a* genotyping.

with Alcian blue. All 3 morphants exhibited similar changes of cartilage layout: a kinked ceratohyal (CH) cartilage and a shortened distance between the Meckel (MK) and CH arches (Figure 6A and Supplemental Figure 3, A and B), a phenotype also reproduced in our *rap1* Cas9/gRNA mutants (Supplemental Figure 3, C and D). Measuring the distance between the MK and CH cartilage along the midline showed that depletion of *rap1*, *kmt2d*, and *kdm6a* significantly decreases the distance between the MK and CH arches ($P < 0.001$; Figure 6B and Supplemental Figure 3B). Moreover, and in agreement with our earlier data, *RAP1A*^{WT} but not *RAP1A*^{R163T} mRNA rescues the jaw phenotype in *rap1* morphants (Figure 6, A and B).

As shown in the ventral view of the jaw layout of 5-dpf embryos (Figure 6A), the CH cartilage of *rap1* and *kmt2d* morphants is shorter and wider compared with control embryos, a phenotype unlikely to be secondary to an overall head-size defect, since the dimension measured was along the anterior-posterior axis that was not grossly affected in our embryos. To explore the cellular basis of this phenotype, we dissected CH arches and evaluated the arrangement of chondrocytes (Figure 6C). Whole-cell counts of the CH arches did not reveal any differences between control embryos and *rap1* and *kmt2d* morphants (Figure 6D), suggesting that the observed anatomical differences were not caused by changes in overall cell number. We therefore considered arrangement defects, and we counted the number of cells between the boundaries of CH arches. In control CH arches, we found an average of 3 to 4 cells between boundaries (Figure 6E). In contrast, CH arches from *rap1* and *kmt2d* morphants contained an average of 5 chondrocytes, a significant difference ($P < 0.0001$; Figure 6E). These data indicated that the observed hypognathia might be caused by a perturbation of cell intercalation, a phenotype consistent with defective CE movements (28). To probe the mechanistic basis of this observation further and to determine whether a rearrangement of the cytoskeleton is involved in cell intercalation (29), we examined whether *rap1* and *kmt2d* are necessary for the formation of the actomyosin network. Utilizing phalloidin and myosin IIa staining, we found that (a) chondrocytes in the CH arch of *rap1* and *kmt2d* morphants fail to line up in a well-organized "fence-like" configuration; (b)

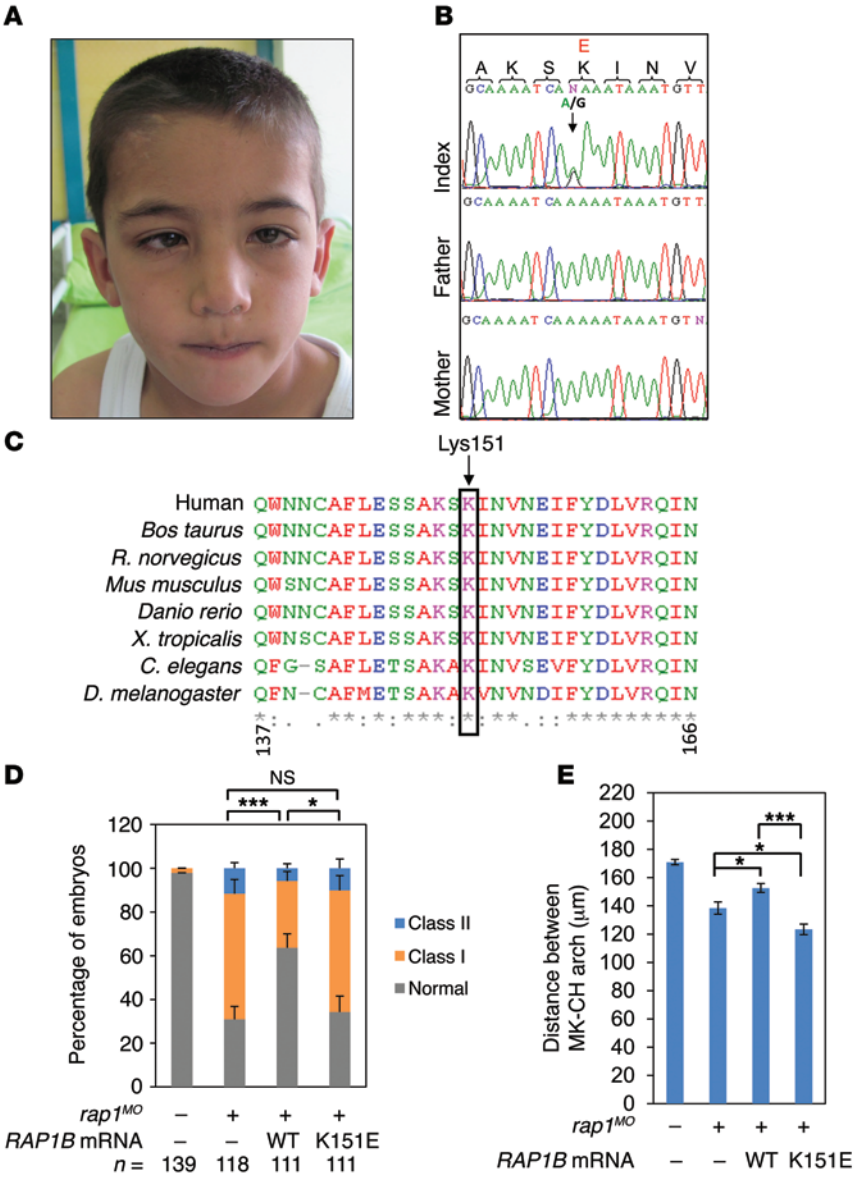

Figure 4. The de novo mutation c.451A>G (p.Lys151Glu) in *RAP1B* identified in a patient with Kabuki-like syndrome. (**A**) Facial features of the patient with the *RAP1B* mutation. (**B**) Sanger sequencing confirmation of the de novo *RAP1B* mutation c.451A>G. (**C**) The affected amino acid residue lysine 151 is highly conserved among a wide range of species. (**D**) In vivo CE complementation assay indicates that *RAP1B* c.451A>G (p.Lys151Glu = K151E) is a loss-of-function mutation. Statistical analysis using the χ^2 test. Error bars show SEM. (**E**) Expression of human *RAP1B* WT mRNA,but not $RAP1B^{K151E}$ mRNA ameliorates the jaw defects in *rap1* zebrafish mutants. Statistical analysis using a 2-tailed Student's *t* test ($n > 20$). $^*P < 0.05$; $^{***}P < 0.001$.

while actin filaments (F-actin) localized mainly at the membrane area of the control cells; this could not been seen in *rap1* and *kmt2d* morphants; and (c) myosin IIa was distributed asymmetrically (polarized) in control embryos but not in *rap1* and *kmt2d* morphants (Supplemental Figure 4A). $RAP1A^{R163T}$ patient fibroblasts stained with phalloidin showed equivalent disorganization of the actin cytoskeleton (Supplemental Figure 4B). We conclude that both the RAP1 and the ASCOM proteins play an important role in actin dynamics and cell intercalation.

Since knockdown (KD) of *rap1* and the known KS genes produced similar cartilage phenotypes, we wondered whether a direct biochemical relationship existed between RAP1 and KMT2D in vivo. Coinjection of subeffective MO doses (Supplemental Figure 5A) for *rap1* and *kmt2d* exacerbated the CE defects of embryos compared with those injected by each single MO ($P < 0.0001$; Figure 7A), raising the possibility that these 2 genes interact genetically. Moreover, expression of $RAP1A^{WT}$ but not $RAP1A^{R163T}$ mRNA rescued the CE defects of *kmt2d* morphants ($P < 0.001$; Figure 7B) as well as the subsequent effects caused by *kmt2d* depletion, such as MAPK hyperactivation and cytoskeleton disorganization (Supplemental Figure 5, B and C), suggesting that RAP1 is downstream of KMT2D. To test whether KMT2D regulates the transcription of the *RAP1* genes (*RAP1A* and *RAP1B*), we assayed the expression of endogenous *rap1a* and *rap1b* in *kmt2d* morphants. Expression levels of *rap1a* were indistinguishable from those of control embryos. However, we saw a significant downregulation of *rap1b* in *kmt2d*-depleted embryos ($P < 0.001$; Figure 7C).

This result argued for a direct relationship between *KMT2D* and *RAP1B*. To explore this possibility further, we performed ChIP in KMT2D haploinsufficient patient fibroblasts. We found that these cells exhibited reduced H3K4 trimethylation at the *RAP1B* promoter and, consequently, a reduced expression of human *RAP1B* (Figure 7, D and E). The RBBP5 protein, a core protein of the ASCOM complex, was found to bind to the *RAP1B* promoter region in WT human fibroblasts (Supplemental Figure 6, A and B), supporting further the direct regulation of *RAP1B* expression by KMT2D.

RAP1 plays opposing roles in the MAPK pathway: as an activator through BRAF and as a repressor through RAF1 (Figure 8A and refs. 19–21). Given the known role of RAP1 in the MAPK pathway, we wondered whether the genetic defects in KS converge on a common pathophysiology governed by altered MEK/ERK signaling. We therefore investigated whether biochemical MEK/ERK defects can be observed in models of KS in vitro and in vivo. First, we examined fibroblasts from the index $RAP1A^{R163T}$ patient. We found a reduced level of phospho-MEK1/2 (pMEK1/2), suggesting that, in this cell type, the p.Arg163Thr allele attenuates the ability of RAP1A to activate MEK/ERK signaling (Figure 8B and Supplemental Figure 7A). The same analysis in fibroblasts from an unrelated patient carrying a mutation in *KMT2D* (c.15079C>T; p.Arg5027*) as well as in lymphoblastoid cell lines (LCLs) from 3 patients with different *KMT2D* mutations (c.15640C>T; p.Arg5214Cys, c.14946G>A; p.Try4982*, and c.13895delC; p.Pro4632Hisfs*8, respectively) showed a similar decrease in MEK and ERK activation (Figure 8, C and D, and Supplemental

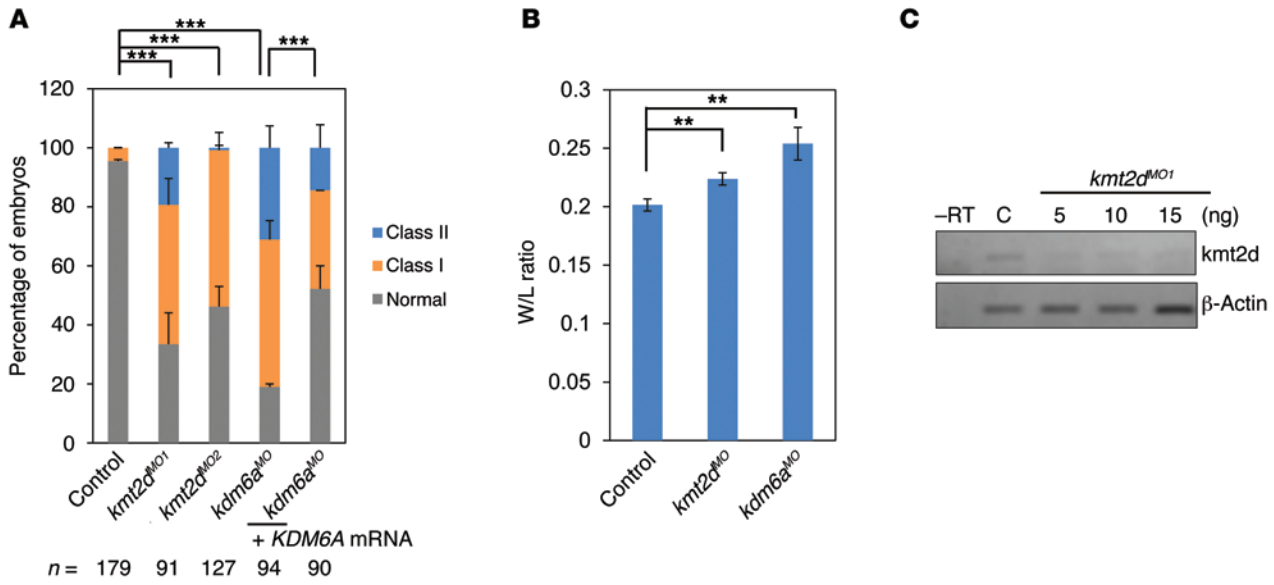

Figure 5. Depletion of *kmt2d* and *kdm6a* affects CE movements in zebrafish embryos. (**A**) Two independent MOs targeting *kmt2d* as well as *kdm6a*^{MO} all result in CE movement defects. Human *KDM6A* mRNA rescues CE defects in *kdm6a* morphants, showing the specificity of *kdm6a*^{MO}. ***$P < 0.001$, χ^2 test. Error bars show SEM. (**B**) Depletion of *kmt2d* and *kdm6a* significantly increases the W/L ratio of somites in midsomatic embryos. Error bars show SEM. **$P < 0.01$, 2-tailed Student's *t* test ($n = 10$). (**C**) RT-PCR for *kmt2d* expression showed efficient KD of *kmt2d* by *kmt2d*^{MO1} ($n = 15$). C, control.

Figure 7, B and C). Additionally, analysis of mouse embryonic fibroblasts (MEFs) derived from *Kmt2d*-KO mice showed the same MEK/ERK signaling defects (Figure 8E and Supplemental Figure 7D). Finally, in addition to reduced active MEK1/2 (Figure 8B), *RAP1A*^{R163T} patient fibroblasts showed a reduction in BRAF phosphorylation, without apparent changes in total BRAF (Figure 9A). Both of these alterations could be rescued by WT *RAP1A* transfection (Figure 9, B and C). Consistent with these data, KD of BRAF in cells derived from a patient with the KMT2D nonsense mutation p.Arg5027* enhanced the reduction of pMEK, while overexpression of *BRAF* increased pMEK levels (Figure 9, D and E). Taken together, these data support the notion that RAP1A acts mainly via activation of BRAF in this cellular context. Coimmunoprecipitation experiments revealed no alterations in the interaction of *RAP1A*^{WT}-GFP or *RAP1A*^{R163T}-GFP with BRAF after EGF stimulation, indicating that the reduced RAP1-mediated BRAF activation in the *RAP1A*^{R163T} fibroblasts is not a result of impaired interaction, but probably of failed RAP1 activation (Figure 9F).

Next, we tested whether the observed pathway defects were also relevant in the in vivo phenotypes of *rap1* morphants. Western blotting of midsomitic whole-embryo lysates showed that suppression of *rap1* during development leads to increased MEK/ERK signaling, which, similarly to in earlier experiments, could not be rescued upon expression of the p.Arg163Thr allele and was phenocopied by suppression of *kmt2d* (Figure 10A). We hypothesized that, in this developmental context, *rap1* is likely to act through inhibition of *raf1* (21) and consequently, that *raf1* hyperactivation would underlie the observed MEK hyperactivation in the *rap1* morphant. If this were true, suppression of *raf1* should rescue the *rap1* morphant phenotype, whereas expression of *BRAF* mRNA should have no effect. Masked analysis of approximately 100 embryos coinjected with MO against *rap1* and either *raf1*^{MO} or *BRAF* mRNA confirmed this hypothesis: *raf1*^{MO} rescued CE ($P < 0.0001$), while expression of WT *BRAF* mRNA did not alter the *rap1* morphant phenotype or the hypognathia of the *rap1* morphants ($P < 0.0001$; Figure 10, B and C, and Supplemental Figure 8, A–C). In addition, depletion of *raf1* also reduced MEK hyperactivation in the *rap1* morphant (Supplemental Figure 8D).

As a result of these findings, we hypothesized that pharmacological treatment of zebrafish embryos with a MAPK agonist should phenocopy the *rap1* morphant phenotype in WT embryos and worsen the phenotype of the *rap1* morphants, while treatment of *rap1*^{MO} embryos with a MAPK antagonist should have an ameliorating effect. We found both predictions to be true. First, injection of embryos with 4 μM of the MAPK agonist PAF-C16 (30) induced CE and hypognathia defects in approximately 50% of embryos and enhanced the CE phenotype of *rap1* morphants when *rap1*^{MO} was coinjected with PAF-C16 (Figure 10, D and E). Second, although injection of the MEK inhibitor PD184161 (31) in WT embryos also induced mild CE defects (Supplemental Figure 8E), it attenuated both the CE defects ($P < 0.0001$; Figure 11A) and the structural cartilage defect in *rap1* morphants, as indicated by the significantly improved distance between the MK and CH arches ($P < 0.001$; Figure 11B). Finally, since we have shown that altered MEK/ERK signaling is also relevant in KMT2D-mediated KS, possibly through the transcriptional regulation of *RAP1B* expression, we speculated that treatment with the MEK inhibitor PD184161 would also ameliorate the phenotypes observed in *kmt2d* morphants. Indeed, we observed significant improvement of the CE and jaw defects in *kmt2d* morphants (Figure 11, C and D).

Discussion

Here, we have shown that *RAP1A* and *RAP1B* contribute to the pathogenesis of KS, the former through the conversion of a heterozygous allele to functional homozygosity by UPD and the latter through a heterozygous germline mutation and as a downstream

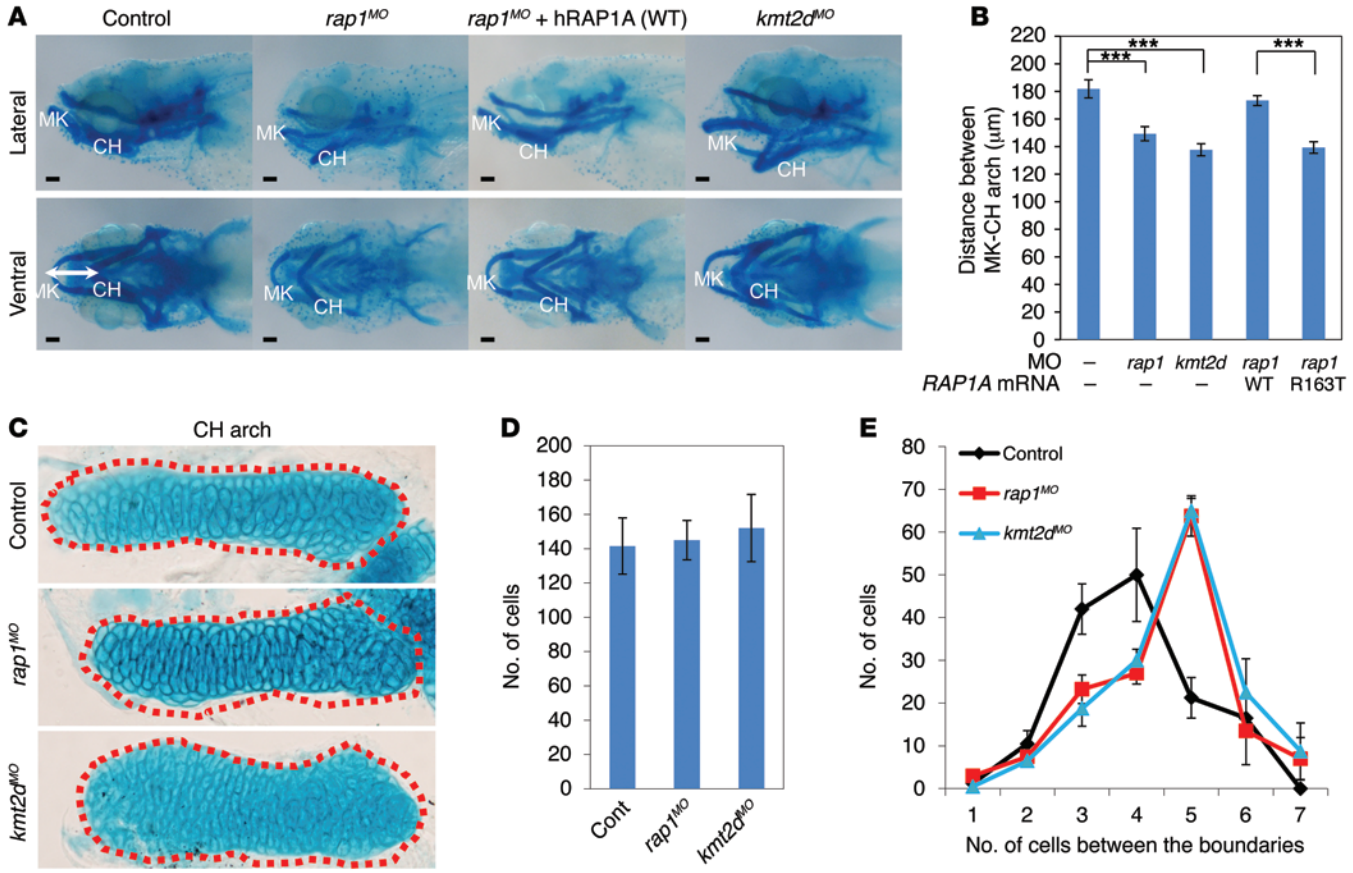

Figure 6. Depletion of *rap1* and *kmt2d* changes the layout of jaw development in 5-dpf zebrafish embryos. (**A**) Alcian blue staining of jaw cartilage. *Rap1* and *kmt2d* morphants have a lower CH arch (lateral view) and shorter distance between MK and CH arches (ventral view; double arrow) in comparison with control embryos. The phenotype is rescued by human WT *RAP1A* mRNA in *rap1* morphants. (**B**) Quantitative measurement of the distance between MK and CH arches. Expression of WT but not $RAP1A^{R163T}$ mRNA rescues the jaw defects in *rap1* morphants. Error bars show SEM. $***P < 0.001$, 2-tailed Student's *t* test ($n = 10$). (**C**) Flat-mount of Alcian blue–stained CH arch. Red dashed line represents the boundary of CH arch. (**D**) Cell number of CH arch is not significantly different between control, *rap1*, and *kmt2d* morphant embryos. Statistical analysis using 2-tailed Student's *t* test ($n = 4$). (**E**) The number of cells between CH arch boundaries is higher in *rap1* and *kmt2d* morphants compared with control embryos ($P < 0.0001$). Statistical analysis using the χ^2 test ($n = 4$). Error bars show SD.

target of KMT2D (and presumably of KDM6A). Although the involvement of *RAP1A* and *RAP1B* is rare, our morphometric and biochemical studies point to a convergence of defects in KS on the MAPK pathway; not only do zebrafish morphants for all 4 KS genes manifest the same anatomical defects, but the biochemical results of in vivo and in vitro analyses are also consistent with this hypothesis. The anatomical and cellular findings suggest further that RAP1 and KMT2D coordinate cell intercalation through the function of polarized actin and myosin IIa. Since skeletal changes are often observed in KS patients, as in the present cases (Table 1), these observations are likely relevant to human pathology.

Chromatin-modifying enzymes such as KMT2D play a fundamental role in cell differentiation and homeostasis during embryonic development and in adult organisms (32–34). The influence of these proteins, and the respective multiprotein complexes such as ASCOM, on chromatin state and gene activation are well analyzed. However, less is known about their downstream effects. Our results shed a light on the cellular mechanisms affected by ASCOM action and dysfunction and link the function of these proteins to the MAPK pathway as one of the major signaling cascades affected in KS.

Activating MAPK pathway mutations, including mutations in both *BRAF* and *RAF1* as well as *MEK1* and *MEK2*, have been found in several RASopathies, including Noonan, Costello, LEOPARD, and cardiofaciocutaneous (CFC) syndromes (35–37), all of which have features that overlap with KS. For example, short stature, developmental delay, skeletal abnormalities, and congenital heart defects can be found in all of these disorders (Supplemental Table 2). Our study suggests that the pathophysiology of KS overlaps with that of the RASopathies. The subcellular defects observed in our study might contribute not only to the skeletal defects in KS, but also to other KS-associated phenotypes, such as heart and renal defects, both of which have been observed in CE mutants with defective cell intercalation (38, 39) and especially in *rap1* morphants (40). Our data also demonstrate that the genetic defects in KS can have opposite effects, either activating or silencing, on the MAPK pathway, depending on whether the RAP1 proteins operate through BRAF or RAF1. These effects, which are likely dependent on cell type and developmental context, might underlie different aspects of the disease. RAP1A loss–mediated hyperactivation of the MAPK pathway impairs the inflammatory response (41). Alter-

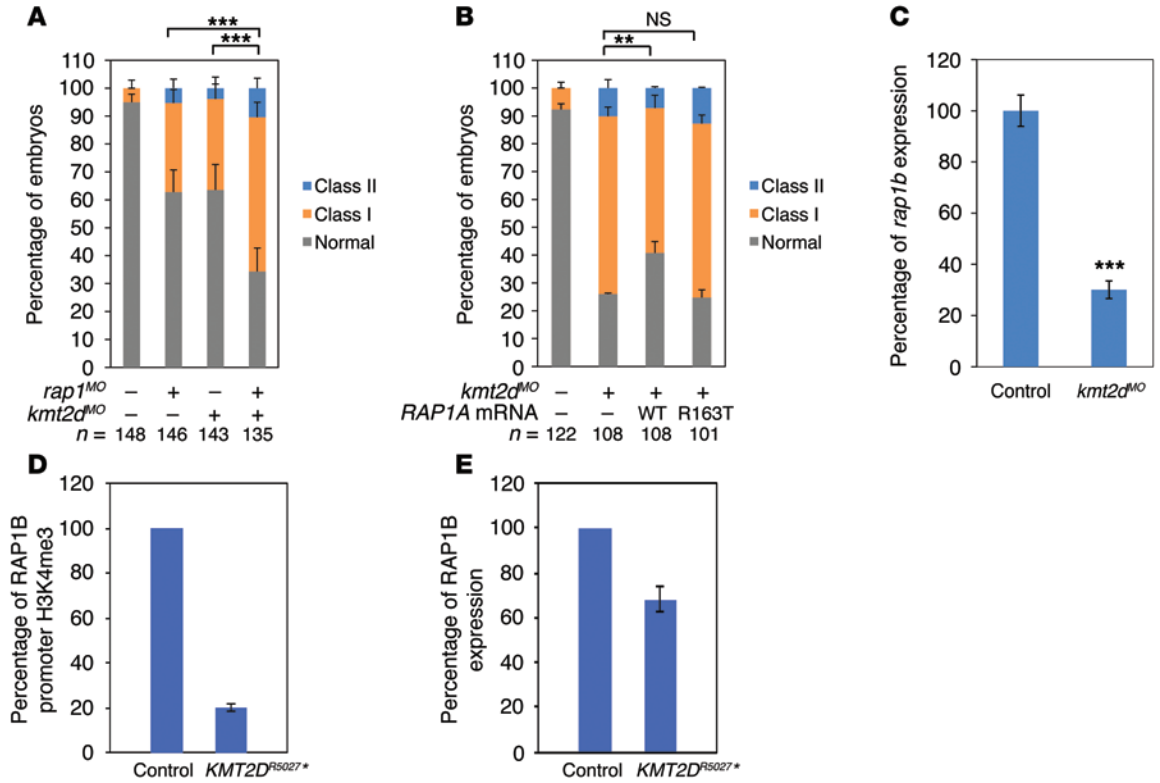

Figure 7. KMT2D regulates the transcription of *RAP1B* in zebrafish and human. (**A**) Coinjection of *rap1*^{MO} with *kmt2d*^{MO} enhances the CE defects in *rap1* morphants. ***$P < 0.001$. (**B**) Expression of WT but not *RAP1A*^{R163T} mRNA rescues CE defects in *kmt2d* morphants. **$P < 0.01$, χ^2 test. Error bars show SEM. (**C**) Real-time RT-PCR from the RNA of 10- to 12-somite stage control and *kmt2d* morphant embryos. MO KD of *kmt2d* reduces the expression of *rap1b*. ***$P < 0.001$, 2-tailed Student's *t* test ($n = 3$). (**D**) ChIP experiments show a marked reduction in H3K4 trimethylation (H3K4me3) of the *RAP1B* promoter in *KMT2D*^{R5027*} patient fibroblasts. Results are given as mean ± SD of all 4 primer pairs used for quantitative PCR for patient and control fibroblast in 1 representative ChIP experiment ($n = 2$). (**E**) Real-time RT-PCR of RNA from the same patient fibroblasts revealed a reduction in *RAP1B* expression. Results are given as mean ± SD of 2 independent experiments for patient and control fibroblasts.

ations in chemotaxis of lymphoid and myeloid cells have been observed in *Rap1a*-KO mice (42). These observations are in line with the increased susceptibility to upper airway tract and middle ear infections as well as different levels of immune deficiencies or autoimmune challenges described in KS patients. Likewise, the MAPK pathway is critical in mediating a host of neurodevelopmental processes through the regulation of gene expression, including neurogenesis and neuronal plasticity (43). We speculate that alterations in these MAPK-driven neuronal processes might underlie impaired cognitive development, which could be accessible to postnatal pharmacological treatment in patients with KS (44). Pharmacological MEK/ERK inhibition at neonatal stages was shown to rescue brain anomalies in an animal model of an Nf1-related RASopathy (45). In our study, we were able to rescue the craniofacial defects in zebrafish models of KS by suppressing *raf1*. Thus, treatment with MAPK-altering drugs might prove beneficial to KS patients. FDA-approved RAF kinase inhibitors such as sorafenib and vemurafenib are presently licensed to treat renal cell carcinoma and melanoma, respectively. Further studies are needed to investigate whether these or novel therapeutic compounds influencing the MAPK pathway could be a practicable therapeutic option for the treatment of several postnatal aspects of the disease, such as cognition, growth, and immune function. Moreover, since the methyltransferases of the KMT2 group as well as the MEK/ERK signaling pathway play an important role in various cancer types (46, 47), the functional link between these 2 systems might help to further promote the understanding of cancer pathogenesis and therapy.

Methods

Patients. We studied 2 nonconsanguineous families of Turkish origin who each had 1 affected child. EDTA blood samples were collected from the 2 affected boys and their parents, and DNA was extracted from peripheral blood lymphocytes by standard extraction procedures. Fibroblasts were obtained from skin biopsies of patients according to standard protocols.

Exome sequencing (trio analysis): RAP1A. Genomic DNA libraries from each of the trio samples were prepared from 3 μg of starting DNA using the Agilent Sure Select Human All Exon 50 Mb Kit (baits are based on the complete annotation of coding regions from the GENCODE project; Agilent Technologies). The resulting fragment libraries, comprising overlapping fragments covering 50 Mb of the exome, were sequenced from both ends (100 bp paired-end sequencing) using Illumina HiSeq 2000 running version 2 chemistry (Illumina). An average of 36 million reads was generated for each sample. Sequence reads were mapped to the reference genome (hg19: GRCh37: Feb2009) using the Burrows-Wheeler Aligner (BWA) (version 0.5.9). The alignment was refined to ensure reads were correctly mapped around

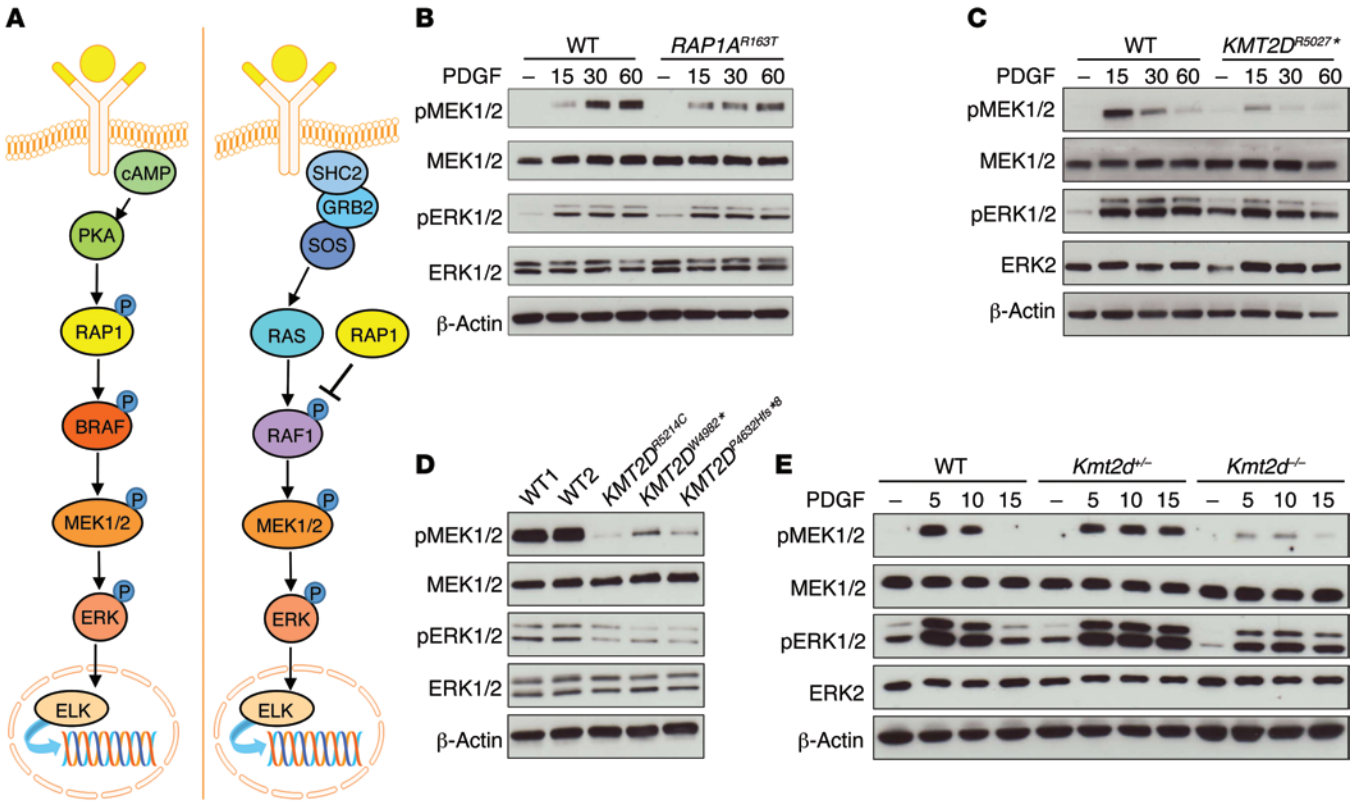

Figure 8. MEK/ERK signaling is perturbed in RAP1A and KMT2D defective cells. (**A**) Schematic representation of MAPK regulation by RAP1. (**B**) Western blot analysis shows reduced phosphorylation of MEK1/2 in *RAP1A*^{R163T} patient fibroblasts after stimulation with PDGF (minutes are indicated; $n = 4$). (**C**) Western blot analysis shows reduced phosphorylation of MEK1/2 and ERK1/2 in patient fibroblasts carrying the KMT2D p.R5027* mutation after stimulation with PDGF (minutes are indicated; $n = 3$). (**D**) Phosphorylation of MEK1/2 and ERK1/2 is reduced in LCLs from 3 different patients with KS carrying confirmed *KMT2D* mutations (c.15640C>T; p.R5214C, c.14946G>A; p.W4982*, and c.13895delC; p.P4632Hfs*8, respectively; $n = 2$). (**E**) Reduced phosphorylation of MEK1/2 and ERK1/2 in primary MEFs from homozygous and heterozygous *Kmt2d*-KO mice after stimulation with PDGF (minutes are indicated; $n = 3$).

insertions and deletions using the Genome Analysis Toolkit (GATK) IndelRealigner (version 1.0.5974). Duplicate reads were marked using Picard (version 1.41) to avoid calling genotypes based on overrepresented library molecules. Base quality scores were then recalibrated using the GATK covariance recalibration tool. An average of 81% of the target exome was covered to 20×, and the mean target coverage in these regions was 64 reads in depth for all samples. SNPs and indels were called using the GATK Unified Genotyper and cross-referenced against known variants from dbSNP132 (http://www.ncbi.nlm.nih.gov/projects/SNP/) and 1KG. A total of 375,937 variations from the reference genome were called after filtering the data according to the GATK Best Practice Variant Detection guidelines (v2). Novel variants in the child were identified using vcftools (v1.0.4a), and the trio was analyzed for violations in Mendelian inheritance using the GATK Select Variants tool. 5,499 novel variants were called in the child, and 595 Mendelian violations were identified. For this analysis, only variants with a coverage greater than 20× were included.

Exome sequencing (trio analysis): RAP1B. Exonic and adjacent intronic regions were enriched from genomic DNA of each patient and his parents using the 50 Mb SureSelect XT Human All Exon Enrichment kit (Agilent Technologies), and sequencing was performed with a HiSeq2000 sequencer from Illumina (Illumina). Alignment against the GRCh37 human reference was performed with the BWA (version 0.6.2), PCR duplicates marking with Picard (version 1.84), indel realignment, base quality recalibration, variant calling with the GATK (version 2.3-4), and annotation with Annovar (version 2013Feb21). The resulting variants were filtered to exclude variants present in dbSNP135, EVS, 1KG, and our in-house database and variants that were not predicted to affect protein sequence or exon splicing. For de novo analysis, all variant loci in the patient's data set were compared with the parental data sets. Only variants covered in all 3 samples and present in less than 5% of the reads in the parental data sets were considered.

Microsatellite marker analysis. Primer sequences (Supplemental Table 3) for 29 microsatellite markers were retrieved from the UCSC genome browser and were purchased from Metabion (Planegg) and IDT DNA. Marker analysis was performed according to standard protocols by PCR amplification and GeneScan on an ABI PRISM 3100 Genetic Analyzer using the GeneScan 500 ROX standard and GeneScan software from Applied Biosystems (Life Technologies).

Sanger sequencing. PCR and sequencing primers (Supplemental Table 3) were retrieved from the UCSC genome browser and purchased from IDT DNA. Sanger sequencing was performed according to standard protocols using the BigDye terminator version 1.1, and carried out on a 3730 sequencer by Applied Biosystems (Life Technologies) at the Cologne Center for Genomics. All coding exons of *RAP1A* were sequenced in 78 patients with KS negative for *KMT2D* mutations and in 115 patients with Noonan syndrome without mutations in the known RASopathy genes.

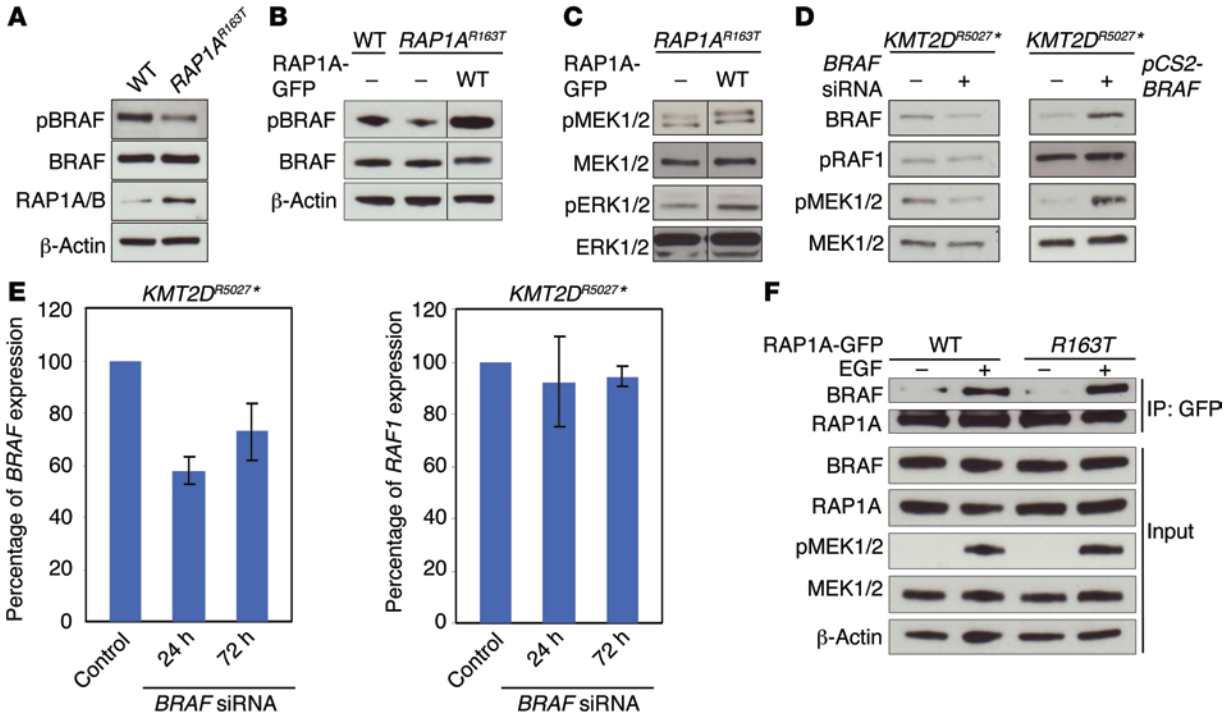

Figure 9. RAP1 signals via BRAF in human adult fibroblasts. (**A**) Activation of BRAF is reduced in *RAP1A*^{R163T} fibroblasts (n = 4). (**B**) Reduced activation of BRAF in patient fibroblasts can be rescued by transfection with WT *RAP1A* (n = 3). (**C**) Reduced activation of MEK1/2 and ERK1/2 in *RAP1A*^{R163T} fibroblasts can be partially rescued by transfection with WT *RAP1A* (n = 2). (**D**) Western blot analysis of siRNA KD of *BRAF* reveals enhanced MAPK signaling defects in KMT2D defective human fibroblasts indicated by further reduction of pMEK (left), whereas the reduced activation of MEK can be rescued by *BRAF* overexpression (right). RAF1 activation reveals no difference upon *BRAF* KD or overexpression in *KMT2D*^{R5027*} fibroblasts (n = 3). (**E**) RT-PCR analysis of *BRAF* (left) and *RAF1* expression (right) upon siRNA KD of *BRAF* after 24 and 72 hours. After 24 hours, *BRAF* expression was about 40% reduced (left). *RAF1* expression levels are independent of *BRAF* expression levels in *KMT2D*^{R5027*} fibroblasts after *BRAF* KD in comparison with mock-treated *KMT2D*^{R5027*} fibroblasts (right). Error bars depict SD (n = 3). (**F**) Coimmunoprecipitation studies revealed no alterations in the interaction of *RAP1A*^{WT}-GFP or *RAP1A*^{R163T}-GFP with BRAF after EGF stimulation (n = 3).

Cell lines and cultures. Patient fibroblasts were derived from skin biopsies of the index patient (RAP1A p.Arg163Thr) and a patient with a KMT2D truncating mutation (p.Arg5027*). Control fibroblasts were obtained from skin biopsy of a healthy individual. MEFs were isolated from *Kmt2d*-KO (*Kmt2d*$^{-/-}$) mouse embryos generated in the Genomics Institute, Bio-Innovationszentrum. Primary human skin fibroblasts and MEFs derived from mice were maintained at 37°C in a 5% CO_2 atmosphere in DMEM medium (Gibco; Life Technologies) supplemented with 10% FBS and antibiotics and subcultured at a 1:2 to 1:5 ratio. LCLs were obtained by EBV-mediated transformation of peripheral blood lymphocytes (according to standard methods) from blood samples of 3 patients with different KMT2D mutations (p.Arg5214Cys, p.Try4982*, and p.Pro4632Hisfs*8, respectively). LCLs were maintained in RPMI medium (Gibco; Life Technologies) supplemented with 10% FBS and subcultured at a 1:2 to 1:4 ratio.

Western blot analysis in human fibroblasts. Patient and control fibroblasts were seeded on 10-cm dishes and maintained in serum-free medium (DMEM containing 0.1% FBS) for 48 hours at 37°C. MEFs were seeded on 10-cm dishes and maintained in serum-free medium for 16 hours at 37°C. At a confluence of 70% to 80%, cells were stimulated with 25 ng/ml recombinant human PDGF-BB (R&D Systems) for the indicated times. For rescue experiments in *RAP1A*^{R163T} patient fibroblasts, we transfected cells with *RAP1A*^{WT}-pEGFP-N1 using Lipofectamin (Life Technologies) according to the manufacturer's instructions. For Western blot analysis of unstimulated LCLs, 2.5×10^6 cells per cell line were taken. Cells were lysed with ice-cold lysis buffer (150 mM NaCl, 1 mM EDTA, 1% NP40, 20 mM Tris-HCl, 0.25% SDS, 1 mM Na_3VO_4, 10 mM NaF, 0.01 mM Na_2MO_4) and treated with benzonase nuclease (Novagen, Merck KGaA). The total protein concentration was determined by using the BCA Protein Assay Kit (Thermo Fisher Scientific), and 10 μg of whole cell lysate per sample was subjected to reducing 4% to 12% SDS-PAGE (Invitrogen, Life Technologies) and transferred to a nitrocellulose membrane by immunoblotting. Immunoblots were blocked in 5% milk powder in TBS containing 0.1% Tween 20 and probed with pBRAF (sc-28006-R; Santa Cruz Biotechnology Inc.), BRAF (F-3, sc-55522; Santa Cruz Biotechnology Inc.), pMEK1/2 (41G9, catalog 9154; catalog 9121; Cell Signaling), MEK1/2 (L38C12, catalog 4694; Cell Signaling), pERK1/2 (catalog 9101; Cell Signaling) or pERK (E-4, sc-7383; Santa Cruz Biotechnology Inc.), total ERK1 (K-23, sc-94; Santa Cruz Biotechnology Inc.) or ERK2 (610103; BD), and total RAP1A/RAP1B (26B4, no. 2399, respectively; Cell Signaling). pERK antibodies detect endogenous levels of p44 and p42 MAP kinases (ERK1 and ERK2) at Thr202 and Tyr204 of ERK1 and Thr185 and Tyr187 of ERK2. The ERK1 antibody detects total ERK1 p44 and, to a lesser extent, ERK2 p42. The ERK2 antibody exclusively detects endogenous levels of p42 MAP kinase (ERK2).

Equal protein amounts were confirmed by β-actin (A 5316; Sigma-Aldrich) detection. Peroxidase-conjugated secondary antibodies (goat anti-mouse: sc-2005, goat-anti-rabbit: sc-2004) were purchased from Santa Cruz Biotechnology Inc., and blots were developed using an enhanced chemiluminescence system, Super Signal West Pico Chemi-

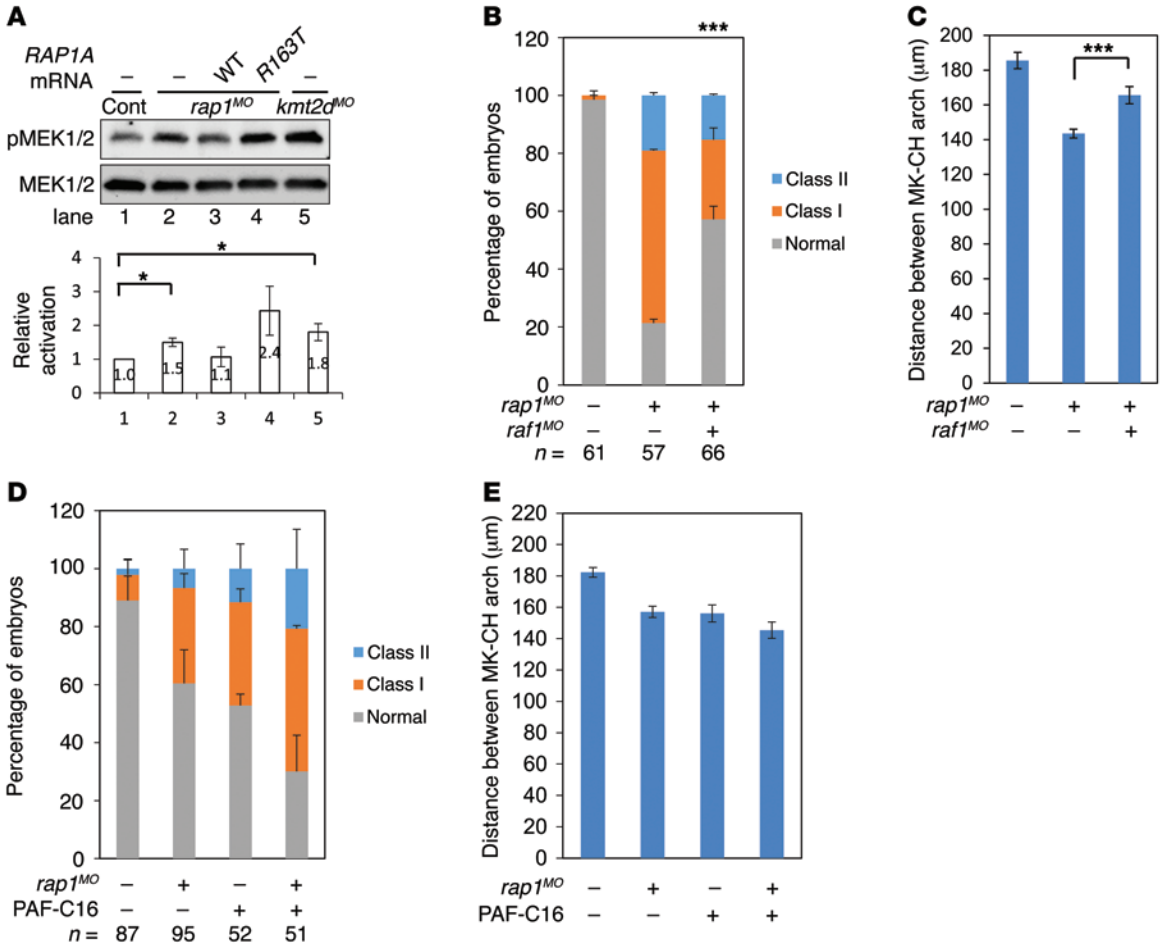

Figure 10. Rap1 signals via RAF1 in early zebrafish development. (**A**) Western blot analysis for the lysates from 10 somites stage (midsomitic stage) zebrafish embryos. Depletion of *rap1* and *kmt2d* elevates the abundance of pMEK1/2 in comparison with control embryos. Expression of WT but not $RAP1A^{R163T}$ mRNA reduces the activation of MEK1/2. Relative level of pMEK abundance is summarized in the lower panel. $^*P < 0.05$, $n = 3$. (**B**) $rap1a^{MO}$ (1 ng) and *rap1b* (1 ng) were injected into embryos. Coinjection of $raf1^{MO}$ ameliorates the CE defects in *rap1* morphants. $^{***}P < 0.001$, χ^2 test. Error bars show SEM. (**C**) Coinjection of $raf1^{MO}$ ameliorates the jaw defects in *rap1* morphants. $^{***}P < 0.001$, 2-tailed Student's *t* test ($n = 10$). (**D**) $rap1a^{MO}$ (0.5 ng) and *rap1b* (0.5 ng) were injected into embryos. MAPK activator PAF-C16 induces CE defects in WT embryos and enhances the CE defects of *rap1* morphants. Statistical analysis using the χ^2 test. Error bars show SEM. (**E**) MAPK activator PAF-C16 enhances the jaw defects in *rap1* morphants. Statistical analysis using a 2-tailed Student's *t* test ($n > 20$). Error bars show SEM.

luminescent Substrate (Thermo Fisher Scientific), followed by exposure on an autoradiographic film (GE Healthcare).

BRAF knockdown and overexpression in human primary fibroblasts. For BRAF knockdown, 1.5×10^5 $KMT2D^{R5027*}$ fibroblasts per transfection sample were seeded on a 6-cm dish 1 day prior to transfection. BRAF knockdown was performed by siRNA transfection. BRAF and nontargeting AllStars Negative Control siRNA serving as mock control were purchased from QIAGEN. 20 μM siRNA stock was diluted to a final concentration of 1 μM. 220 μl of the 1 μM siRNA dilution was mixed with 220 μl Opti-MEM (Life Technologies), and 4.4 μl DharmaFECT 1 (Thermo Fisher Scientific) was mixed with 435.6 μl Opti-MEM; both mixtures were incubated separately for 5 minutes at room temperature (RT), mixed, and again incubated for 20 minutes at RT. Medium was removed from cells, and 3.5 ml DMEM medium containing 10% FCS and no antibiotics was added. Then the siRNA mixture (final concentration of 50 nM) was added onto the cells. After 24 hours, RNA was directly isolated for RT-PCR analysis or cells were treated as before by serum starvation in medium containing 0.1% FCS for an additional 48 hours. After a total of 72 hours, RNA was directly isolated for RT-PCR analysis (Quantitect primer assay from QIAGEN for BRAF, RAF1, actin) or cells were treated with 25 ng/ml PDGF for 15 minutes and total cell lysates were subjected to Western blot analysis.

For *BRAF* overexpression, 1×10^5 $KMT2D^{R5027*}$ fibroblasts per transfection sample were seeded in 6-well plates 1 day prior to transfection. *BRAF* overexpression was performed by transfection of pCS2-BRAF. 500 ng DNA was mixed with 3.6 μl FuGENE HD Transfection Reagent (Promega) in a total of 200 μl Opti-MEM according to the manufacturer's instructions and added onto the cells with 1.8 ml fresh DMEM. After 24 hours, cells were lysed and total lysates were subjected to Western blot analysis. Immunoblots were blocked in 5% milk powder in TBS containing 0.1% Tween 20 and probed with BRAF (F-3, sc-55522, Santa Cruz Biotechnology Inc.), pRAF1 (56A6, catalog 9427, Cell Signaling), pMEK1/2 (41G9, catalog 9154, Cell Signaling), and MEK1/2 (L38C12, catalog 4694, Cell Signaling).

Active Rap1 pull-down assay. Detection of active RAP1A was performed using the Active RAP1 Pull-Down and Detection Kit (Thermo

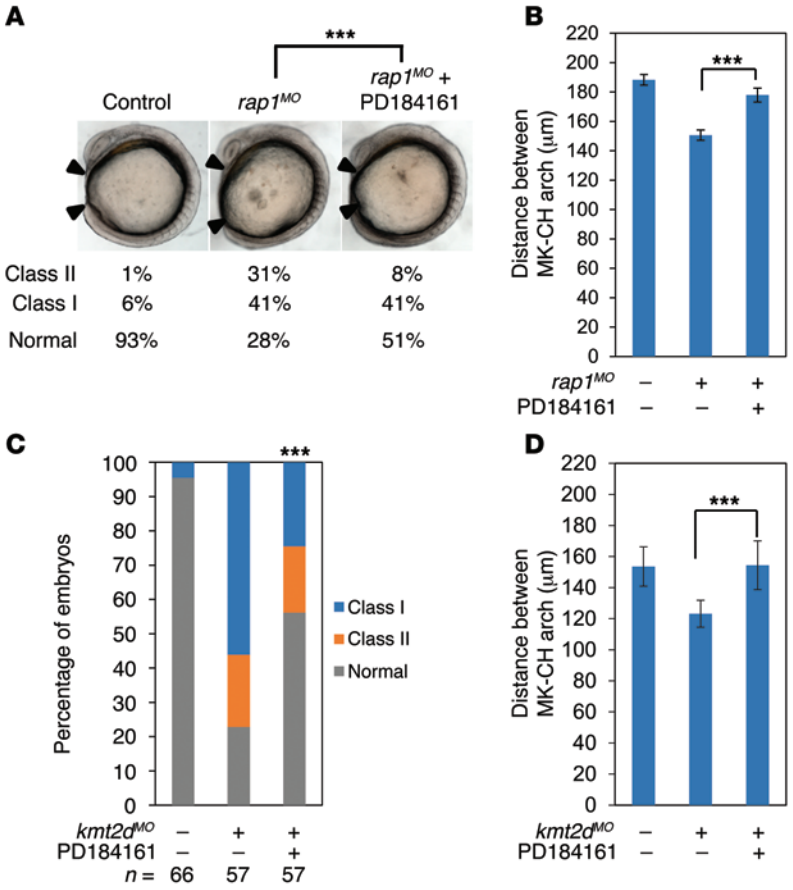

Figure 11. MEK/ERK signaling alterations can be rebalanced by pharmacological treatment in zebrafish models of KS. (**A**) Coinjection of MEK inhibitor PD184161 ameliorates the CE defects in *rap1* morphants. ***$P < 0.001$, χ^2 test ($n > 80$). (**B**) Coinjection of MEK inhibitor PD184161 ameliorates the jaw defects in *rap1* morphants. ***$P < 0.001$, 2-tailed Student's *t* test ($n = 10$). (**C**) Coinjection of PD184161 ameliorates the CE defects in *kmt2d* morphants. ***$P < 0.001$, χ^2 test. (**D**) Coinjection of PD184161 ameliorates the jaw defects in *kmt2d* morphants. ***$P < 0.001$, 2-tailed Student's *t* test ($n = 10$). Error bars show SEM.

Fisher Scientific) according to the manufacturer's instructions. In brief, HEK293T cells were plated in 10-cm dishes 24 hours prior to transfection. Transient transfections were performed with FuGene-HD (Roche) according to the manufacturer's instructions with the expression constructs for GFP-tagged WT human *RAP1A* and the p.Arg163Thr mutant. One day after transfection, cells were starved in serum-free medium for 24 hours, stimulated with 100 ng/ml recombinant human EGF (R&D Systems) for 5 minutes, and lysed. The total protein concentration was determined using the BCA Protein Assay Kit (Thermo Fisher Scientific), and 200 μg of whole cell lysate per sample was subjected to active RAP1A pull-down.

ChIP assay and quantitative PCR. To quantify *RAP1B* promoter H3K4 trimethylation, primary fibroblasts of the patient (*KMT2D*^{R5027*}) and a healthy control individual were seeded on 10-cm dishes. ChIP was performed based on the manufacturer's instructions (ChIP Assay Kit, Millipore) with the following changes: histones were crosslinked to DNA with a final concentration of 1% formaldehyde in fresh culture medium for 10 minutes at RT. The formaldehyde reaction was quenched by adding glycine to 125 mM for 4 minutes at RT. To shear DNA to lengths between 200 and 1000 bp, lysates were sonicated at 4°C for 16 cycles (30 s ON, 30 s OFF, high power; BioRuptor, Diagenod). Precleared lysates were incubated overnight with 2 μg of the immunoprecipitation (IP) antibody H3K4me3 (ab8580, Abcam) at 4°C with rotation. An additional sample without antibody served as a negative control for quantitative PCR. To collect the antibody-histone-DNA complex, 60 μl of protein A agarose/salmon sperm DNA (50% slurry) was incubated for 1.5 hours at 4°C with rotation. DNA was recovered by phenol/chloroform extraction and ethanol precipitation.

The quantitative PCR for *RAP1B* promoter H3K4 trimethylation was based on amplification of H3K4 trimethylated *RAP1B* promoter regions in relation to an internal reference promoter region of the *HOX7A* gene (*KMT2D*-independent H3K4 trimethylation) using the QuantiFast SYBR Green PCR Kit (QIAGEN). A total of 4 different primer pairs for 2 different promoter regions of the *RAP1B* gene and 1 primer pair for a promoter region of *HOX7A* were designed (methylation sites of *RAP1B* and *HOX7A* promoters were previously published, ref. 48). Primer sequences are presented in Supplemental Table 3. Real-time PCR was conducted 2 times for each primer pair and DNA sample. Each reaction had 20 μl volume containing 10 μl of 2× QuantiFast SYBR Green PCR Master Mix, 250 nM of the primers, and 5 ng of recovered DNA after ChIP procedure. Thermal cycling was performed for 10 minutes at 95°C and then 40 cycles for 15 seconds at 95°C and for 1 minute at 60°C, followed by a final dissociation stage. The comparative method of relative quantification ($2^{\Delta\Delta Ct}$) was used to calculate the relative H3K4me3 level of the *RAP1B* promoter in patient fibroblasts (normalized to *HOX7A*) in comparison with control fibroblasts. Results are given as mean ± SD of all 4 primer pairs for patient and control fibroblasts. The IP sample without antibody incubation served as a negative control.

To assay binding of the ASCOM complex at the described H3K4 regions of the *RAP1B* promoter, primary fibroblasts of a healthy control individual were seeded on 10-cm dishes. ChIP was performed based on the manufacturer's instructions (ChIP Assay Kit, Millipore) with the described changes of the protocol. Precleared lysates were incubated overnight with a dilution of 1:50 of the IP antibody RBBP5 (D3I6P, catalog 13171, Cell Signaling) at 4°C with rotation. An additional sample without antibody served as a negative control for nonquantitative PCR analysis.

Real-time RT-PCR in patient fibroblasts. Total RNA from primary fibroblasts of the patient (*KMT2D*^{R5027*}) and a healthy control individual was purified using the RNeasy Mini Kit (QIAGEN). For homogenization of cell lysates, QIAshredder spin columns were used (QIAGEN). Real-time RT-PCR for *RAP1B* expression analysis was performed using the Power SYBR Green RNA-to-C_T 1-Step Kit (Applied Biosystems, Life Technologies). QuantiTect Primer Assays for *RAP1B* and *ACTB* RNA as an internal control were purchased from QIAGEN. Each reaction had 20 μl volume containing 10 μl of 2× Power SYBR Green RT-PCR Mix, 0.15 μl RT Enzyme Mix, 2 μl of QuantiTect primer and 25 ng RNA as template. Thermal cycling was performed for 30 minutes at 48°C (reverse transcription step), for 10 minutes at 95°C, and then 40 cycles for 15 seconds at 94°C, and for 30 seconds at 60°C and 35 seconds at 72°C, followed by a final dissociation stage. Real-time RT-PCR was con-

ducted 3 times for each gene and RNA sample. The comparative method of relative quantification ($2^{\Delta\Delta Ct}$) was used to calculate the relative expression level of *RAP1B* in patient fibroblasts (normalized to *ACTB*) in comparison with control fibroblasts. Results are given as mean ± SD of 2 independent experiments for patient and control fibroblasts.

Microinjection of MO, mRNA, Cas9/gRNA, and MEK drugs in zebrafish embryos. MOs used in this study were purchased from Gene Tools (Gene Tools LLC). The injection amounts were as follows: *rap1a*: 1 ng; *rap1b*: 1 ng; *kmt2d*^{MO1}: 5 ng; *kmt2d*^{MO2}: 5 ng; *kmd6a*: 10 ng; *raf1*: 2.5 ng. See Supplemental Table 3 for sequences. The open reading frames of the human genes were inserted into a pCS2 vector, and the mRNAs were synthesized with the SP6 mMessage mMachine kit (Ambion, Life Technologies). The injection amounts of mRNAs were as follows: *RAP1A* (WT or p.Arg163Thr): 0.5 pg; and *KDM6A*: 100 pg. CRISPR target sequences (Supplemental Table 3) were identified by crispr.mit.edu. and cloned into pT7-gRNA (Addgene) following the manufacturer's protocol (http://www.addgene.org/crispr/Chen/). gRNAs and *Cas9* mRNA (pCS2-nCas9n; Addgene) were synthesized using the T7 and Sp6 mMessage mMachine kit (Ambion). 120 pg gRNA plus 150 pg *Cas9* mRNA were injected into zebrafish embryos at the 1-cell stage. PD184161 and PAF-C16 (Santa Cruz Biotechnology Inc.) were dissolved in DMSO and diluted further with water to the final concentration: PD184161 (500 pM) and PAF-C16 (4 μM). As indicated in the text, MO, MO in combination with mRNA, or MO in combination with drugs was injected into WT zebrafish embryos at the 1- to 4-cell stage. Embryos were scored as previously described (24) at the 8- to 10-somite stage, and images were captured using Nikon AZ100 and NIS Elements software. Pairwise comparisons to WT for rescue efficiency were conducted using a χ^2 test. All experiments were conducted with a minimum of 2 independent injections in embryo clutches from different parents, scored using the same criteria, and always blinded to injection cocktails.

Whole-mount in situ hybridization and cartilage staining. From 10- to 12-somite stage embryos were fixed with 4% paraformaldehyde (PFA) overnight. Whole-mount in situ hybridization was carried out as described (26) with a mix of riboprobes (*krox2*, *myoD*, and *pax2*). Yolk sacs of embryos were then removed and whole mounted with glycerol. Images were captured with Nikon SMZ745T (Nikon), and the W/L ratio was obtained by ImageJ (http://imagej.nih.gov/ij/). To assess the jaw layout, Alcian blue staining for cartilage structure was performed in 5-dpf embryos following the procedure as described (27). Fish embryos were imaged in glycerol using Nikon SMZ745T. The distance between MK and CH arches were then measured with ImageJ. To obtain the detailed image of the CH arch, after Alcian blue staining, CH cartilages were cut from whole embryos and incubated with protease K (10 μg/ml; Invitrogen, Life Technologies) for 30 minutes, followed by flat mount with 3% methyl cellulose. The images were taken using a Nikon 90i, Nikon digital sight camera and NIS Elements software. Pairwise comparisons of *rap1* and *kmt2d* morphants to control embryos for cell intercalation were conducted using a χ^2 test. To assess the actin network of cartilage cells, 5-dpf embryos were fixed in 4% PFA overnight, followed by methanol dehydration and rehydration. Embryos were then incubated with Phalloidin-TRITC (1 μg/ml; P1951, Sigma-Aldrich) for 1 hour, followed by DAPI staining for 5 minutes, or with Myosin IIa (3403S, Cell Signaling) at a concentration of 1:100 at 4°C overnight. The confocal images were captured using a Zeiss 710 confocal microscope. Pictures of 3 embryos for each condition were taken.

Real-time PCR in zebrafish embryos. Total RNA from 10- to 12-somite stage embryos was extracted with TRIzol (Invitrogen, Life Technologies) following the manufacturer's protocol. cDNA was synthesized from 1 μg of total RNA using SuperScript III (Invitrogen). To investigate *rap1a* and *rap1b* expression of *kmt2d* morphants, real-time PCR was performed with Power SYBR Green PCR Master Mix (Applied Biosystems, Life Technologies) on a 7900HT (Applied Biosystems). To obtain the absolute concentration of *raf1* and *braf* expression, serial dilutions of the PCR products of *raf1* and *braf* were used as standards in real-time PCR. Real-time data were collected and analyzed with a Sequence Detection System software package version 2.3 (Applied Biosystems). Primer sequences are presented in Supplemental Table 3.

Western blot analysis of zebrafish embryos. 10- to 15-dpf embryos were lysed in RIPA buffer (50 mM Tris [pH 7.5], 1% NP-40, 0.1% SDS, 50 mM NaCl, 0.5% Na deoxycholate, 1 mM NaF). After electrophoresis and transferring, the blots were incubated with antibodies as indicated in the figures (pMEK1/2: 1:1000; MEK1/2: 1:3000; Rap1: 1:1000; actin: 1:3000) at 4°C overnight. The images of Western blot were taken by Chemidoc (Bio-Rad) and quantified by Quantity One software (Bio-Rad).

Accession numbers. The following gene reference sequences can be found at http://www.ncbi.nlm.nih.gov/nuccore: *RAP1A*, NM_001010935.2; *RAP1B*, NM_015646.5; *KMT2D*, *MLL2*; NM_003482.3; *KDM6A*, NM_021140.3.

Statistics. All results are expressed as the mean ± SD or SEM. All data were analyzed using a 2-tailed Student's *t* test or the χ^2 test. $P < 0.05$ was considered statistically significant.

Study approval. We obtained written informed consent from all patients and probands for participation in this study. We obtained written informed consent from the index families for publication of photographs. The study was performed according to the Declaration of Helsinki protocols and was approved by the Ethics Committee of the University of Cologne. The zebrafish experiments were approved by the Ethics Board of Duke University.

Acknowledgments

We are grateful to all family members that participated in this study and Karin Boss for critically reading the manuscript. This work was supported by the German Federal Ministry of Education and Research (BMBF), by grants 01GM1211A (E-RARE network CRANIRARE-2) and 01GM1109C (national rare disease network FACE) to B. Wollnik, by grant 01GM1211B (E-RARE network CRANIRARE-2) to D. Wieczorek, by TÜBİTAK grant 112S398 to H. Kayserili, by NIH grants R01DK075972 and P50DK096415 to N. Katsanis, by NRSA fellowship F32DK094578 to I-C. Tsai, and by Else Kröner-Fresenius-Stiftung 2012_A300 to A.F. Stewart and A. Kranz.

Address correspondence to: Bernd Wollnik, Institute of Human Genetics, University Medical Faculty, University of Cologne, Kerpener Str. 34, 50931 Cologne, Germany. Phone: 49.221.478.86817; E-mail: bwollnik@uni-koeln.de. Or to: Nicholas Katsanis, Center for Human Disease Modeling, 466A Nanaline Duke Building, Box 3709, Duke University Medical Center, Durham, North Carolina 27710, USA. Phone: 919.613.4694; E-mail: katsanis@cellbio.duke.edu.

1. Bögershausen N, Bruford E, Wollnik B. Skirting the pitfalls: a clear-cut nomenclature for H3K4 methyltransferases. *Clin Genet*. 2013;83(3):212–214.
2. Ng SB, et al. Exome sequencing identifies MLL2 mutations as a cause of Kabuki syndrome. *Nat Genet*. 2010;42(9):790–793.
3. Lederer D, et al. Deletion of KDM6A, a histone demethylase interacting with MLL2, in three patients with Kabuki syndrome. *Am J Hum Genet*. 2012;90(1):119–124.
4. Miyake N, et al. KDM6A point mutations cause Kabuki syndrome. *Hum Mutat*. 2013;34(1):108–110.
5. Bögershausen N, Wollnik B. Unmasking Kabuki syndrome. *Clin Genet*. 2013;83(3):201–211.
6. Paulussen AD, et al. MLL2 mutation spectrum in 45 patients with Kabuki syndrome. *Hum Mutat*. 2011;32(2):E2018–E2025.
7. Banka S, et al. Novel KDM6A (UTX) mutations and a clinical and molecular review of the X-linked Kabuki syndrome (KS2). *Clin Genet*. 2015;87(3):252–258.
8. Schuettengruber B, Martinez A-M, Iovino N, Cavalli G. Trithorax group proteins: switching genes on and keeping them active. *Nat Rev Mol Cell Biol*. 2011;12(12):799–814.
9. Ruthenburg AJ, Allis CD, Wysocka J. Methylation of lysine 4 on histone H3: intricacy of writing and reading a single epigenetic mark. *Mol Cell*. 2007;25(1):15–30.
10. Cho Y-W, Hong S, Ge K. Affinity purification of MLL3/MLL4 histone H3K4 methyltransferase complex. *Methods Mol Biol*. 2012;809:465–472.
11. Cho YW, et al. PTIP associates with MLL3- and MLL4-containing histone H3 lysine 4 methyltransferase complex. *J Biol Chem*. 2007;282(28):20395–20406.
12. Agger K, et al. UTX and JMJD3 are histone H3K27 demethylases involved in HOX gene regulation and development. *Nature*. 2007;449(7163):731–734.
13. Micale L, et al. Molecular analysis, pathogenic mechanisms, and readthrough therapy on a large cohort of Kabuki syndrome patients. *Hum Mutat*. 2014;35(7):841–850.
14. Jossin Y, Cooper JA. Reelin, Rap1 and N-cadherin orient the migration of multipolar neurons in the developing neocortex. *Nat Neurosci*. 2011;14(6):697–703.
15. Parkinson K, et al. Regulation of Rap1 activity is required for differential adhesion, cell-type patterning and morphogenesis in Dictyostelium. *J Cell Sci*. 2009;122(pt 3):335–344.
16. Suh HN, Han HJ. Laminin regulates mouse embryonic stem cell migration: involvement of Epac1/Rap1 and Rac1/cdc42. *Am J Physiol Cell Physiol*. 2010;298(5):C1159–C1169.
17. Tsai I-C, Amack JD, Gao Z-H, Band V, Yost HJ, Virshup DM. A Wnt-CKIvarepsilon-Rap1 pathway regulates gastrulation by modulating SIPA1L1, a Rap GTPase activating protein. *Dev Cell*. 2007;12(3):335–347.
18. Bos JL, de Rooij J, Reedquist KA. Rap1 signalling: adhering to new models. *Nat Rev Mol Cell Biol*. 2001;2(5):369–377.
19. Vossler MR, Yao H, York RD, Pan MG, Rim CS, Stork PJ. cAMP activates MAP kinase and Elk-1 through a B-Raf- and Rap1-dependent pathway. *Cell*. 1997;89(1):73–82.
20. York RD, et al. Rap1 mediates sustained MAP kinase activation induced by nerve growth factor. *Nature*. 1998;392(6676):622–626.
21. Hu CD, Kariya Ki, Kotani G, Shirouzu M, Yokoyama S, Kataoka T. Coassociation of Rap1A and Ha-Ras with Raf-1 N-terminal region interferes with ras-dependent activation of Raf-1. *J Biol Chem*. 1997;272(18):11702–11705.
22. Lo IF, Cheung LY, Ng AY, Lam ST. Interstitial Dup(1p) with findings of Kabuki make-up syndrome. *Am J Med Genet*. 1998;78(1):55–57.
23. Franke B, et al. Sequential regulation of the small GTPase Rap1 in human platelets. *Mol Cell Biol*. 2000;20(3):779–785.
24. Leitch CC, et al. Hypomorphic mutations in syndromic encephalocele genes are associated with Bardet-Biedl syndrome. *Nat Genet*. 2008;40(4):443–448.
25. Jao L-E, Wente SR, Chen W. Efficient multiplex biallelic zebrafish genome editing using a CRISPR nuclease system. *Proc Natl Acad Sci U S A*. 2013;110(34):13904–13909.
26. Sarmah S, Barrallo-Gimeno A, Melville DB, Topczewski J, Solnica-Krezel L, Knapik EW. Sec24D-dependent transport of extracellular matrix proteins is required for zebrafish skeletal morphogenesis. *PLoS One*. 2010;5(4):e10367.
27. Zoeller JJ, et al. A central role for decorin during vertebrate convergent extension. *J Biol Chem*. 2009;284(17):11728–11737.
28. Tada M, Heisenberg CP. Convergent extension: using collective cell migration and cell intercalation to shape embryos. *Development*. 2012;139(21):3897–3904.
29. Skoglund P, Rolo A, Chen X, Gumbiner BM, Keller R. Convergence and extension at gastrulation require a myosin IIB-dependent cortical actin network. *Development*. 2008;135(14):2435–2444.
30. Chen Z, Rola-Pleszczynski M, Stankova J. Activation of ERK1/2 by platelet-activating factor receptor is independent of receptor internalisation and G-protein activation. *Cell Signal*. 2003;15(9):843–850.
31. Klein PJ, et al. The effects of a novel MEK inhibitor PD184161 on MEK-ERK signaling and growth in human liver cancer. *Neoplasia*. 2006;8(1):1–8.
32. Hu D, Gao X, Morgan MA, Herz H-M, Smith ER, Shilatifard A. The MLL3/MLL4 branches of the COMPASS family function as major histone H3K4 monomethylases at enhancers. *Mol Cell Biol*. 2013;33(23):4745–4754.
33. Lee JE, et al. H3K4 mono- and di-methyltransferase MLL4 is required for enhancer activation during cell differentiation. *Elife*. 2013;2:e01503.
34. Kim DH, Lee J, Lee B, Lee JW. ASCOM controls farnesoid X receptor transactivation through its associated histone H3 lysine 4 methyltransferase activity. *Mol Endocrinol*. 2009;23(10):1556–1562.
35. Lee BH, Kim JM, Jin HY, Kim GH, Choi JH, Yoo HW. Spectrum of mutations in Noonan syndrome and their correlation with phenotypes. *J Pediatr*. 2011;159(6):1029–1035.
36. Tartaglia M, Gelb BD. Disorders of dysregulated signal traffic through the RAS-MAPK pathway: phenotypic spectrum and molecular mechanisms. *Ann N Y Acad Sci*. 2010;1214:99–121.
37. Tidyman WE, Rauen KA. The RASopathies: developmental syndromes of Ras/MAPK pathway dysregulation. *Curr Opin Genet Dev*. 2009;19(3):230–236.
38. Yu H, Ye X, Guo N, Nathans J. Frizzled 2 and frizzled 7 function redundantly in convergent extension and closure of the ventricular septum and palate: evidence for a network of interacting genes. *Development*. 2012;139(23):4383–4394.
39. Lienkamp SS, et al. Vertebrate kidney tubules elongate using a planar cell polarity-dependent, rosette-based mechanism of convergent extension. *Nat Genet*. 2012;44(12):1382–1387.
40. Dong W, et al. Suppression of Rap1 impairs cardiac myofibrils and conduction system in zebrafish. *PLoS One*. 2012;7(11):e50960.
41. Dorn A, et al. Rap1a deficiency modifies cytokine responses and MAPK-signaling in vitro and impairs the in vivo inflammatory response. *Cell Immunol*. 2012;276(1–2):187–195.
42. Li Y, et al. Rap1a null mice have altered myeloid cell functions suggesting distinct roles for the closely related Rap1a and 1b proteins. *J Immunol*. 2007;179(12):8322–8331.
43. Impey S, Obrietan K, Storm DR. Making new connections: role of ERK/MAP kinase signaling in neuronal plasticity. *Neuron*. 1999;23(1):11–14.
44. Bjornsson HT, et al. Histone deacetylase inhibition rescues structural and functional brain deficits in a mouse model of Kabuki syndrome. *Sci Transl Med*. 2014;6(256):256ra135.
45. Wang Y, et al. ERK inhibition rescues defects in fate specification of Nf1-deficient neural progenitors and brain abnormalities. *Cell*. 2012;150(4):816–830.
46. Morin RD, et al. Frequent mutation of histone-modifying genes in non-Hodgkin lymphoma. *Nature*. 2011;476(7360):298–303.
47. Parsons DW, et al. The genetic landscape of the childhood cancer medulloblastoma. *Science*. 2011;331(6016):435–439.
48. Ke XS, et al. Genome-wide profiling of histone h3 lysine 4 and lysine 27 trimethylation reveals an epigenetic signature in prostate carcinogenesis. *PLoS One*. 2009;4(3):e4687.
49. Li Y, et al. A mutation screen in patients with Kabuki syndrome. *Hum Genet*. 2011;130(6):715–724.
50. Matsumoto N, Niikawa N. Kabuki make-up syndrome: a review. *Am J Med Genet C Semin Med Genet*. 2003;117C(1):57–65.